# Coherent Combination of GPS III L1 C/A and L1C Signals for GNSS Reflectometry

Hao Du, *Graduate Student Member, IEEE*, Yang Nan, Weiqiang Li, *Senior Member, IEEE*, Estel Cardellach, *Senior Member, IEEE*, Serni Ribó, *Member, IEEE*, and Antonio Rius

***Abstract*— With the evolution of global navigation satellite systems (GNSSs), more GNSS satellites and civilian signals are available for GNSS reflectometry (GNSS-R). Developments of new onboard processing strategies can improve the observation performance of spaceborne GNSS-R. To this end, this article proposes a new processing method by coherently combining reflected global positioning system (GPS) III level 1 (L1) C/A and L1C signals. By exploiting the additional signal component, the signal-to-noise ratio (SNR) of the reflected signal can be significantly improved. Moreover, by taking advantage of the narrower autocorrelation function of the combined signal, the spatial resolution and the performance of geophysical applications can be significantly improved. The proposed method has been validated by processing cyclone GNSS (CYGNSS) raw intermediate frequency data, including the direct and reflected signals from GPS III satellites. The results indicate that the SNR of the combined reflected waveform can be improved by ∼2 dB compared to the L1 C/A waveform. Moreover, the SNR of the combined signal can be improved more efficiently using a longer coherent integration interval compared to the L1 C/A signal. Preliminary altimetric results demonstrate a 35.3%–61.6% improvement in the ranging standard deviation and a 22.4%–64.4% improvement in the median absolute deviation compared to L1 C/A measurements. In addition, the correlation coefficient between combined measurements and wind speed improves by 26.3% on average compared to L1 C/A measurements and 45.7% for high winds. This article presents a novel GNSS-R onboard signal processing method with improved performance, which can provide a reference for the design of future GNSS-R instruments.**

Manuscript received 31 July 2023; revised 28 November 2023 and 3 March 2024; accepted 6 May 2024. Date of publication 8 May 2024; date of current version 21 May 2024. This work was supported in part by MCIN/AEI/10.13039/501100011033 with contributions from the "European Union Next Generation EU/PRTR" under Grant RYC2019-027000-I, Grant PID2021-126436OB-C22, and Grant CEX2020-001058-M; in part by the Spanish National Research Council under Grant 20215AT007; and in part by the National Natural Science Foundation of China under Grant 42304017. This work of Hao Du was supported in part by the China Scholarship Council (CSC) through a State Scholarship Fund under Grant 202206270011. *(Corresponding author: Weiqiang Li.)*

Hao Du is with the Earth Observation Research Group, Institute of Space Sciences (ICE), Spanish National Research Council (CSIC), 08193 Barcelona, Spain, also with the Institut d'Estudis Espacials de Catalunya, 08034 Barcelona, Spain, and also with the Faculty of Earth Sciences, University of Barcelona, 08028 Barcelona, Spain.

Yang Nan is with the School of Marine Science and Technology, Tianjin University, Tianjin 300072, China.

Weiqiang Li, Estel Cardellach, Serni Ribó, and Antonio Rius are with the Earth Observation Research Group, Institute of Space Sciences (ICE), Spanish National Research Council (CSIC), 08193 Barcelona, Spain, and also with the Institut d'Estudis Espacials de Catalunya, 08034 Barcelona, Spain (e-mail: weiqiang@ice.csic.es).

Digital Object Identifier 10.1109/TGRS.2024.3398435

***Index Terms*— Coherent combination, global navigation satellite system reflectometry (GNSS-R), global positioning system (GPS) III, L1C signal, ocean altimetry, ocean scatterometry, sea surface wind speed.**

## I. Introduction

As a novel passive remote sensing technique, the spaceborne global navigation satellite system reflectometry (GNSS-R) has rapidly developed over the past few decades. It relies on signals transmitted by GNSS satellites and only requires the receiver part. The basic theory and applications of this technique are comprehensively introduced in [1], [2], and [3]. Its main advantages include low cost, global coverage, high temporal and spatial resolution, and short revisit time, e.g., [4]. Furthermore, the L-band GNSS signals have exceptional penetrating capabilities in heavy rain and cloud cover, e.g., [5].

Since the time remote sensing using Earth-reflected global positioning system (GPS) signals was conceived, e.g., [6] and [7], numerous ground-based and airborne experiments have been conducted to demonstrate its feasibility, e.g., [8], [9], and [10]. In 2003, the first spaceborne GNSS-R demonstration experiment onboard the U.K. Disaster Monitoring Constellation (DMC) satellite was performed [11]. The received level 1 (L1) C/A reflected signals were used for sea surface altimetry, e.g., [12], roughness retrieval, e.g., [13], ice detection, e.g., [14], and other applications. The U.K. TechDemoSat-1 (TDS-1) followed, providing more GNSS-R measurements from reflected L1 C/A signals [15]. As a milestone of the GNSS-R development, NASA's 8 microsatellites' constellation cyclone GNSS (CYGNSS) was launched in 2016 and provides GNSS-R measurements from March 2017 [16]. The CYGNSS mission was designed to monitor high wind speeds near the center of tropical cyclones. In addition, other geophysical applications have been also demonstrated with the CYGNSS data products, e.g., sea surface height [17], [18], [19], water mask [20], mean sea slope [21], heat flux [22], soil moisture [23], soil freeze/thaw [24], [25], [26], and sea surface microplastic concentration [27]. The two most commonly applied techniques are conventional GNSS-R (cGNSS-R) and interferometric GNSS-R (iGNSS-R) [4]. As for iGNSS-R, the reflected signal is cross-correlated with the direct signal, and multiple types of ranging code can be processed with no need to generate local replicas. However, a high-gain antenna

is necessary for iGNSS-R, so this technique is generally used in the ground-based receiver due to the limitation of the receiver size. On the other hand, the reflected GNSS signals are correlated with the local replica in cGNSS-R, and the requirement for the antenna gain is lower. Therefore, cGNSS-R is more suitable for spaceborne GNSS-R receivers although only ranging codes whose sequence is known can be processed, such as GPS L1 C/A and L1C. However, most efforts for developing cGNSS-R up to now are based on processing GPS L1 C/A signals. It is necessary to develop new cGNSS-R processing methods for modernized GNSS signals.

GNSS constellations have been evolving and developing to improve positioning, navigation, and timing (PNT) services in the past years. The new GNSS constellations, such as Galileo and BeiDou, increase the available sources of measurements and, thus, can further improve the temporal and spatial coverage for GNSS-R applications. In addition, new civil signals, such as GPS L1C and L5, Galileo E1C, and E5A/B, are modulated using binary offset carrier (BOC) and have a narrower correlation peak compared to binary phase shift keying (BPSK) signals. In modernized GNSS signals, multiple signal components are modulated at the same frequency, providing the possibility of different processing and observation strategies. Therefore, the GNSS-R onboard processing algorithms should adapt to the new signals to take full advantage of the technique and, thus, improve the performances in different applications. Up until now, many spaceborne GNSS-R constellations have been or will be launched, which can process GNSS signals other than L1 C/A, such as Bufeng-1 [28] for L1/B1, Fengyun-3 [29] and Spire GNSS-R [30] for L1/E1/B1, FSSCat for E1 [31], and HydroGNSS for L1/E1 and L5/E5A [32].

As for the modernized GPS, the first GPS III satellite was launched on December 23, 2018, and began service on January 9, 2019 [33]. Currently, there are six GPS III satellites in service up-to-date. While the BPSK modulated L1 C/A signal is retained to ensure compatibility with existing processing strategies, the new civilian signals, such as L1C signals, are also modulated by BOC with the same carrier as the L1 C/A signal. The L1C signal consists of data (L1Cd) and pilot (L1Cp) components with BOC(1,1) and time-multiplexed BOC(6,1,4/33) modulations [34]. Due to the limited bandwidth of most of the spaceborne GNSS-R receivers, only the BOC(1, 1) component in L1Cd and L1Cp signals can be received. Different from the triangle shape of the BPSK autocorrelation function (ACF), the BOC ACF has two negative side peaks besides the main peak, which can reduce the width of the ACF and reduce the multipath effects in traditional PVT applications. There have been a few studies on reflectometry using modernized GNSS signals. Jales [35] explored a coherent signal addition scheme for Galileo E1B and E1C BOC(1, 1) components in 2012. The signal-to-noise ratio (SNR) was improved by 3 dB compared to that using the incoherent addition. In 2020, Wang and Juang [36] proposed composite delay-Doppler maps (DDMs) using simulated L1 C/A and L1C signals by the open-source GNSS-R simulator Wavpy [37] based on the configuration of the upcoming TRITON mission. The results show that the root mean square error (RMSE) of wind speed retrieved by three composite DDM observables is approximately 1 m/s, while the state-of-the-art RMSE of CYGNSS wind speed products is about 1.19 m/s [38]. This provides a way to remove the noise without complicated power calibration. However, L1 C/A and L1C DDMs are combined after being incoherently averaged, which cannot efficiently increase the SNR. In 2022, Li et al. [39] provide an overview of up-to-date spaceborne GNSS-R raw intermediate frequency (IF) datasets and corresponding processing methods. The Institute of Space Sciences [ICE-Spanish National Research Council (CSIC)/Institut d'Estudis Espacials de Catalunya (IEEC)] published postprocessed data products including the complex waveform (cWF) of the direct and reflected L1 C/A signals, carrier phase, and metadata, using TDS-1, CYGNSS, Bufeng-1, and Spire GNSS radio occultation raw IF datasets. By applying the same processing strategy, the cWF of GPS III satellites can be generated including both the C/A code and the L1C signal components.

Considering the autocorrelation properties of L1 C/A and L1C signals, this article proposes a new processing method that combines them coherently. Specifically, 1-ms coherently correlated cWFs of L1 C/A, L1Cd, and L1Cp are combined to generate a new combined waveform, which can improve GNSS-R observation performance. The rest of this article is organized as follows. Section II introduces the autocorrelation characteristics of L1 C/A and L1C signals, as well as the proposed coherent combination method. In Section III, the proposed method is implemented in the processing of direct and reflected signals collected by the CYGNSS satellites. Theoretical improvements of the combined waveforms are analyzed and validated by the measured data. The improvements in ocean altimetry and wind speed retrieval are validated and analyzed in Section IV. Finally, the conclusions and outlooks are provided in Section V.

## II. GPS III Signal Properties and Data Processing

In order to explain the principle behind combining GPS III L1 C/A and L1C signals, their mathematical expressions and characteristics will be explained in this section. In addition, the CYGNSS raw IF data of GPS III and its processing method are illustrated in detail.

### A. Properties of GPS III L1 C/A and L1C Signals

The L1 band (centered at 1575.42 MHz) signals transmitted by modernized GPS III satellites partially consist of L1 C/A and L1C signal components, which can be expressed as

$$S_{\mathrm{L1}}(t) = \sqrt{P_{\mathrm{CA}}}S_{\mathrm{CA}}(t) + j\left[\sqrt{P_{\mathrm{Cd}}}S_{\mathrm{Cd}}(t) + \sqrt{P_{\mathrm{Cp}}}S_{\mathrm{Cp}}(t)\right] \tag{1}$$

where $P_{\mathrm{CA}}$, $P_{\mathrm{Cd}}$, and $P_{\mathrm{Cp}}$ are the powers of three components and $S_{\mathrm{CA}}$, $S_{\mathrm{Cd}}$, and $S_{\mathrm{Cp}}$ are the pseudorandom noise (PRN) modulated signal components before correlation. Detailed information on different signal components is provided in Table I.

The ideal L1 C/A signal with an infinite bandwidth is modulated using BPSK(1) with its ACF defined approximately

TABLE I

SUMMARY OF GPS L1 C/A AND L1C SIGNALS [34], [40]

| Code type | L1 C/A | L1C | |
|---|---|---|---|
| | | L1Cd | L1Cp |
| Modulation | BPSK(1) | BOC(1, 1) | TMBOC(6, 1, 4/33) |
| Code length | 1023 | 10230 | 10230 |
| Period (ms) | 1 | 10 | 10 |
| Minimum received power (dBW) | -158.5 | -163.0 | -158.25 |
| Bandwidth (MHz) | 2.046 | 4.092 | |

as

$$R_{\mathrm{CA}}(\tau)=\begin{cases}1-\dfrac{|\tau|}{T_{\mathrm{chip}}}, & |\tau|<T_{\mathrm{chip}}\\ 0, & \text{else}\end{cases} \tag{2}$$

where $\tau$ is the code delay and $T_{\mathrm{chip}}$ is the time length of a code chip.

As for the L1C signal, the modulation mode of the L1Cp component is TMBOC(6, 1, 4/33) defined as

$$S_{\mathrm{L1Cp}}=\frac{29}{33}\mathrm{BOC}(1,1)+\frac{4}{33}\mathrm{BOC}(6,1). \tag{3}$$

However, due to the limited bandwidth of the GNSS-R instrument onboard the CYGNSS satellites, the BOC(6,1) component is filtered, and the BOC(1, 1) component is also filtered significantly due to the shape of its power spectrum. Received L1Cd and L1Cp signals only contain the BOC(1, 1) component. The ideal ACF of BOC(1, 1) signals with an infinite bandwidth is defined as

$$R_{\mathrm{L1C}}(\tau)=\begin{cases}1-\dfrac{3|\tau|}{T_{\mathrm{chip}}}, & |\tau|<\dfrac{T_{\mathrm{chip}}}{2}\\ \dfrac{|\tau|}{T_{\mathrm{chip}}}-1, & \dfrac{T_{\mathrm{chip}}}{2}<|\tau|<T_{\mathrm{chip}}\\ 0, & \text{else.}\end{cases} \tag{4}$$

Other datasets from airborne and ground-based platforms did receive signals with broader bandwidths [10], which could be used to experiment with the full L1C components. This is left for future work and not included in this study.

The L1 C/A and L1C signal components are modulated at the same carrier signal, and the phases of the cWFs from different signal components should be also coherent. In addition, as shown in Fig. 1, there are two negative side peaks in the BOC(1, 1) ACF, where the ACF value of L1 C/A is numerically equal but inverse to that of L1C. Consequently, by combining L1C and L1 C/A signals, the combined ACF is limited within $[-T_{\mathrm{chip}}/2, T_{\mathrm{chip}}/2]$. If the power ratio between L1 C/A and L1C signals is about 1:1, the ideal combined ACF shown in Fig. 1 is defined as

$$\begin{aligned}R_{\mathrm{com}}(\tau)&=\frac{1}{2}R_{\mathrm{L1\ C/A}}(\tau)+\frac{1}{2}R_{\mathrm{L1C}}(\tau)\\&=\begin{cases}1-\dfrac{2|\tau|}{T_{\mathrm{chip}}}, & |\tau|<\dfrac{T_{\mathrm{chip}}}{2}\\ 0, & \text{else.}\end{cases}\end{aligned} \tag{5}$$

It is noted that $S_{\mathrm{CA}}$ has a 90° phase shift to $S_{\mathrm{Cd}}$ and $S_{\mathrm{Cp}}$ because L1 C/A and L1C components are modulated quadrature and in phase, respectively [34], [40]. When combining them coherently, their phase difference should be taken into account.

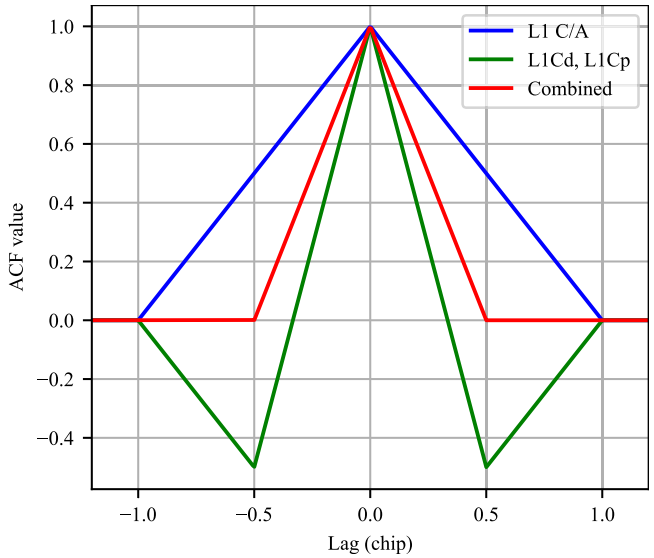


Fig. 1. Ideal ACFs of the GPS L1 C/A BPSK(1), L1C BOC(1, 1), and their combination. For $T_{\mathrm{chip}}/2<|\tau|<T_{\mathrm{chip}}$, the ACF value of L1 C/A is numerically equal but inverse to that of L1C. Thus, by combining L1C to L1 C/A signals, the side peaks are removed and the width of the combined ACF can reduce to $[-T_{\mathrm{chip}}/2, T_{\mathrm{chip}}/2]$.

In reality, the receiver bandwidth is not infinite, and the received L1 C/A and L1C signals are filtered accordingly. Thus, the combined ACF in Fig. 1 and (5) may change for different receiver bandwidths. According to Table I, the minimum received power ratio between L1 C/A and BOC(1, 1) components in L1Cd and L1Cp signals is about 0.44:0.16:0.40. Thus, the amplitude ratio between BPSK(1) and BOC(1, 1) components is about 1:1.128. To analyze the influence of the receiver bandwidth, ACFs of BPSK(1) and BOC(1, 1) are filtered by different bandwidths with a peak ratio of 1:1.128. As shown in Fig. 2, the ACFs of BPSK(1) and BOC(1, 1) filtered by 2.0, 2.5, 4.0, and 10.0 MHz and infinite bandwidths are compared. Due to the shape of the power spectrum, BOC(1, 1) signals lose more information if the bandwidth is lower than 4 MHz. When the bandwidth is 2.5 MHz, the ratio of the ACF peak between BPSK(1) and BOC(1, 1) is about 1:0.96. For convenience, it can be regarded as 1:1 so that the combining method in (5) can be still applied when the receiver bandwidth is 2.5 MHz.

Then, BPSK(1) and BOC(1, 1) ACFs are added with the ratio of 1:1, as shown in Fig. 3, and the filtered BPSK(1), BOC(1, 1), and combined ACF peaks, as well as the amplitude and power ratio between the combined and BPSK(1) ACFs, are given in Table II. With the bandwidth increasing, the combined ACF peak also increases mainly benefiting from the decreasing power loss of the BOC(1, 1) signal. When the bandwidth reaches up to 10.0 MHz, the shape of the combined ACF is similar to that with the infinite bandwidth. In this article, the main concern is the situation with the receiver bandwidth of 2.5 MHz. The ratio between combined and BPSK(1) ACF peaks is about 1.96, and the power ratio is its square, i.e., 3.84. Although side peaks exist, their amplitudes are very

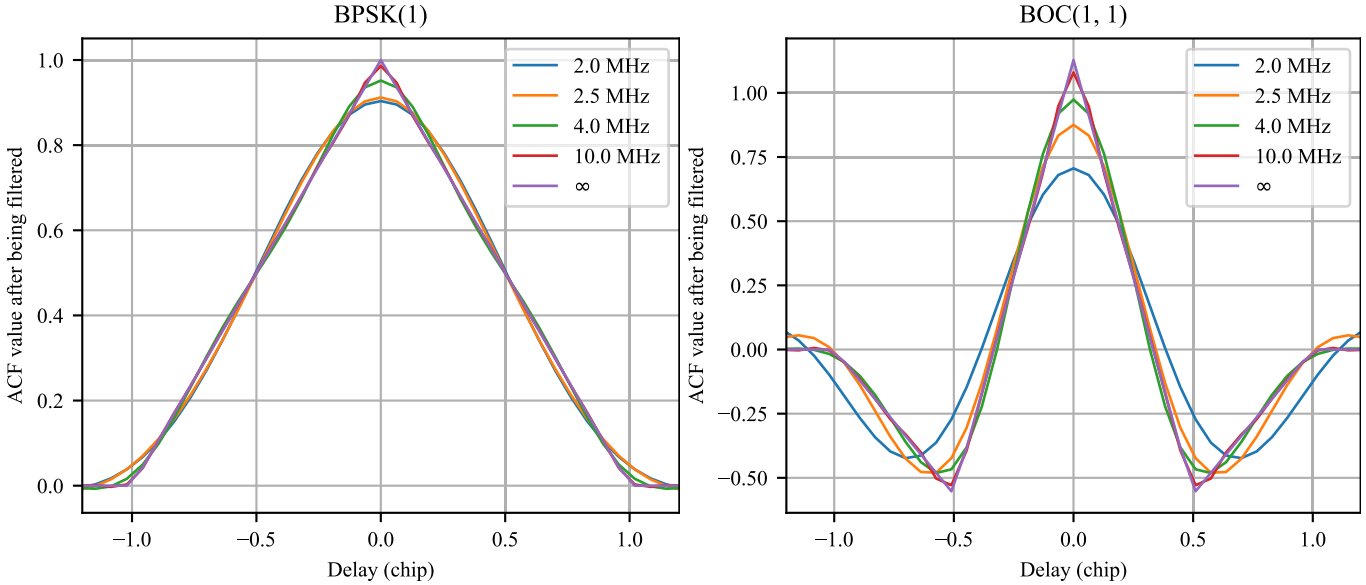


Fig. 2. ACFs of BPSK(1) (left) and BOC(1, 1) (right) signals with different bandwidths. When the bandwidth is 2.5 MHz, the ACF peak values of BPSK(1) and BOC(1, 1) are 0.912 and 0.875, respectively.

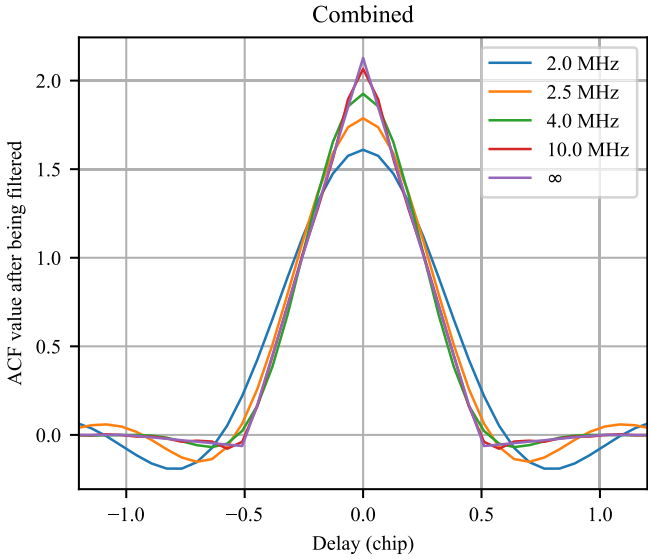


Fig. 3. ACFs of combined waveforms with the combination coefficient as 1:1. The filtered peak ACF value with the 2.5-MHz bandwidth is about 1.787.

small, and they will not influence the combination a lot. As for different receiver bandwidths, the combination coefficients can be redesigned to ensure the equal amplitude of BPSK(1) and BOC(1, 1) signals according to their ACF peak ratios given in Table II.

### B. CYGNSS Raw IF Data Processing

Raw IF data are processed using the GNSS-R software receiver to obtain GPS III L1 C/A and L1C cWFs. This section presents the CYGNSS dataset and raw IF data processing method.

*1) Dataset:* CYGNSS selectively provides raw IF direct and reflected signal data to explore specific events [41], such as hurricanes and frozen lakes. Each raw IF data file contains a 30–60-s raw signal sample stream received by both zenith

TABLE II

ACF PEAKS OF BPSK(1), BOC(1, 1), COMBINED SIGNALS, AND AMPLITUDE AND POWER RATIOS BETWEEN COMBINED AND BPSK(1) SIGNALS WITH DIFFERENT BANDWIDTHS

| Bandwidth (Mhz) | ACF peak | | | Amplitude ratio | Power ratio |
|---|---|---|---|---|---|
| | BPSK(1) | BOC(1, 1) | Combined | | |
| 2.0 | 0.904 | 0.706 | 1.610 | 1.78 | 3.17 |
| 2.5 | 0.912 | 0.875 | 1.787 | 1.96 | 3.84 |
| 4.0 | 0.952 | 0.974 | 1.926 | 2.02 | 4.08 |
| 10.0 | 0.986 | 1.080 | 2.067 | 2.09 | 4.37 |
| ∞ | 1.000 | 1.128 | 2.128 | 2.13 | 4.54 |

and nadir antennas. The bandwidth of the raw signals is approximately 2.5 MHz centered at around 3.8 MHz. Real sampling is applied with the sampling rate of 16.0362 MHz, and the quantizer resolution is 2 bits. With the 2.5-MHz bandwidth, the BOC(6, 1) component in L1Cp signals and the partial BOC(1, 1) component in L1Cd and L1Cp signals are filtered out. Finally, only the partial BOC(1, 1) component in L1C signals can be obtained from CYGNSS raw IF data. In order to calculate the position of the specular point (SP), it is necessary to collect the orbits and altitude information of GPS transmitters and CYGNSS receivers. GPS transmitters' positions are calculated using multi-GNSS experiment (MGEX) data from the International GNSS Service (IGS) [42]. CYGNSS L1 data [43] contain the orbit and altitude information of the receivers.

The datasets during 2019–2022 are processed to obtain GPS III signals reflected from the ocean surface. There are a total of 23 sets of raw IF collections over the ocean, which include the signals transmitted by the GPS III satellites. After removing the tracks with low SNR (as discussed in Section III), we only keep 15 tracks of GNSS-R data from GPS III satellites with their information presented in Table III and their ground tracks shown in Fig. 4.

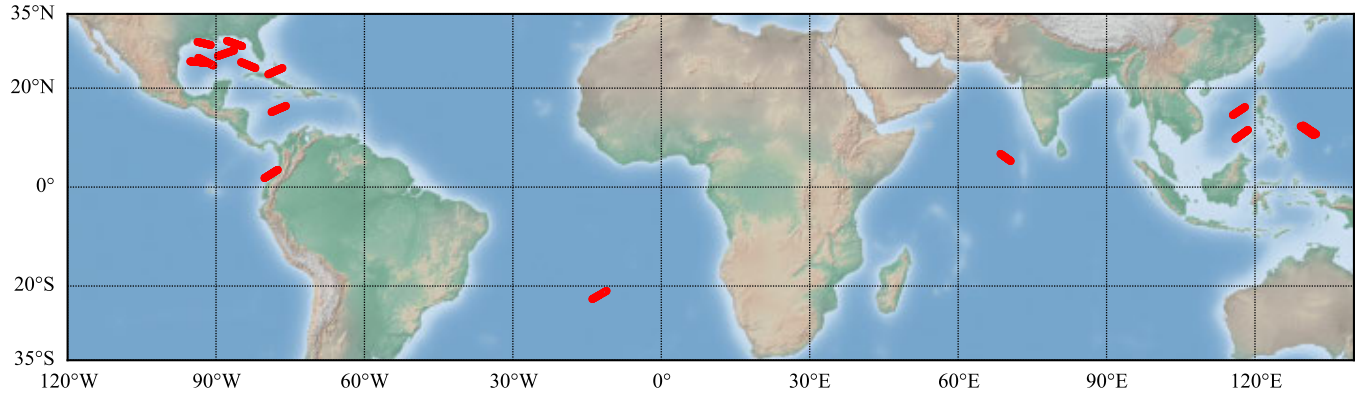


Fig. 4. Spatial distribution of the processed GPS III reflected signals. There are a total of 15 tracks used later in the performance analysis of the combined waveforms.

TABLE III
BASIC INFORMATION OF 15 TRACKS OF PROCESSED GPS III RAW IF DATA

| Track ID | Date | FM* | GPS PRN | Lat (°) | Lon (°) | Incidence angle (°) | Filtered samples | $\overline{SNR_{CA}}$ (dB) | $\overline{SNR_{CP}}$ (dB) |
|---|---|---|---|---|---|---|---|---|---|
| 1 | 20200621 | cyg07 | G18 | [-22.6, -21.0] | [14.0, 11.1] | 34.9 | 36-39 | 0.75 | -2.46 |
| 2 | 20200912 | cyg08 | G04 | [28.7, 29.3] | [-93.8, -91.0] | 40.1 | 0-12 | 1.97 | -0.32 |
| 3 | 20201008 | cyg02 | G23 | [24.6, 26.1] | [-93.6, -90.5] | 36.6 | 43-46 | 1.17 | -1.54 |
| 4 | 20201112 | cyg01 | G18 | [9.7, 11.6] | [116.0, 118.6] | 26.7 | 2,3 | 0.45 | -2.03 |
| 5 | 20201112 | cyg01 | G23 | [14.5, 16.2] | [115.5, 118.0] | 57.5 | 0-4 | -3.89 | –6.38 |
| 6 | 20210414 | cyg03 | G23 | [5.3, 6.7] | [68.6, 70.6] | 44.0 | 2-4 | -1.00 | -3.01 |
| 7 | 20210417 | cyg01 | G14 | [10.7, 12.5] | [129.7, 132.4] | 39.3 | 27-30 | -3.65 | -4.94 |
| 8 | 20210417 | cyg02 | G14 | [10.5, 12.3] | [129.2, 131.9] | 29.4 | 32-34 | -2.81 | -4.14 |
| 9 | 20211020 | cyg02 | G04 | [25.0, 25.4] | [-95.2, -91.8] | 69.6 | – | -0.51 | -2.69 |
| 10 | 20220214 | cyg02 | G14 | [28.5, 29.6] | [-87.8, -84.7] | 55.0 | – | -5.89 | -8.27 |
| 11 | 20220303 | cyg01 | G18 | [26.5, 27.6] | [-89.6, -86.4] | 26.4 | – | 6.48 | 3.28 |
| 12 | 20220317 | cyg07 | G14 | [1.8, 3.5] | [-80.2, -77.5] | 71.7 | – | 7.15 | 4.92 |
| 13 | 20220319 | cyg03 | G14 | [22.8, 24.1] | [-79.4, -76.6] | 30.6 | – | 4.08 | 1.23 |
| 14 | 20220422 | cyg01 | G18 | [15.2, 16.4] | [-78.8, -75.9] | 62.4 | – | -2.65 | -5.46 |
| 15 | 20220504 | cyg04 | G23 | [24.1, 25.2] | [-84.9, -82.0] | 57.0 | – | -5.89 | -7.32 |

* FM: flight model or CYGNSS satellite

*2) Raw IF Data Processing:* The main raw IF data processing follows [39] with the addition of L1C signal processing, which consists of closed-loop processing of the GPS L1 C/A direct signal and open-loop processing of the direct L1C signal and the reflected L1C and L1 C/A signals. The auxiliary parameters, such as the positions, velocities, and timing information of the GPS transmitters and CYGNSS receivers, are extracted from the corresponding GPS precise ephemeris files and CYGNSS L1 data.

The L1 C/A direct signal is demodulated based on a generic GNSS signal processing following [44]. The code offset $\psi_d(t)$, carrier frequency $f_d(t)$, and carrier phase $\phi_d(t)$ are estimated after signal acquisition and tracking by a delay-locked loop and a phase-locked loop, generating the time series of $[\psi_d(t), f_d(t), \phi_d(t)]$. A third-degree polynomial function is then implemented to smooth the time series and reduce random tracking errors. As the GPS L1 C/A code signal and the L1C signals are synchronized with their code phases and modulated at the same carrier signal, the code phase, carrier frequency, and carrier phase of the L1C signal can be computed directly from those of the GPS L1 C/A code signal. With those parameters, the received direct signals $s_d(t)$ are cross-correlated with the local carrier and PRN code replicas generated using the smoothed code offset $\psi_d(t)$, carrier frequency $f_d(t)$, and phase $\phi_d(t)$. The cWFs of different signal components in the direct signal can be expressed as

$$z_d^X(t_0,\tau) = \int_{-T_c/2}^{T_c/2} s_d^X(t_0+t_c)c^X[\psi_d(t_0+t_c)+\tau] \times e^{-j2\pi[f_d(t_0)t_c+\phi_d(t_0)]}dt_c \tag{6}$$

where the superscript $^X$ denotes the signal components, i.e., C/A, L1Cd or L1Cp, $t_0$ is the epoch of the direct waveform, $c(\cdot)$ is the local PRN code replica, and $T_c$ is the coherent integration time, which is set as 1 ms for all the signal components.

The open-loop processing for the reflected signal components is based on the same processing strategy in [19]. The code offset $\psi_r(t)$, carrier frequency $f_r(t)$, and phase $\phi_r(t)$ of the reflected signals can be computed through

$$\begin{aligned} \psi_r(t) &= \psi_d(t) - \delta\tau(t)\cdot f_{\text{code}} \\ \phi_r(t) &= \phi_d(t) - \delta\tau(t)\cdot f_c \\ f_r(t) &= f_d(t) - \frac{\partial}{\partial t}\delta\tau(t)\cdot f_c \end{aligned} \tag{7}$$

where $\delta\tau(t) = \delta\rho(t)/c$ is the time delay difference between the direct and reflected signals, $f_{\text{code}} = 1.023$ MHz, and $f_c = 1575.42$ MHz for both L1 C/A and L1C signals.

With the code and carrier parameters computed from (7), the cWF of the reflected signal $s_r^X(t)$ is also generated by

cross-correlating with the code and carrier replicas

$$z_r^X(t_0,\tau)=\int_{-T_c/2}^{T_c/2}s_r^X(t_0+t_c)c^X[\psi_r(t_0+t_c)+\tau]\times D^X[t_0+t_c-\delta\tau(t_0)]e^{-j2\pi\left[f_r(t_0)t_c+\phi_r(t_0)\right]}dt_c \quad (8)$$

where the coherent time $T_c$ is also set as 1 ms, the superscript $^X$ denotes the signal components, i.e., C/A, L1Cd or L1Cp, and $D^X$ is the navigation data bits or the secondary code obtained from the direct signal cWFs in (6). Thus far, the L1 C/A, L1Cd, and L1Cp direct and reflected 1-ms cWFs are generated and can be combined coherently.

## III. Implementation, Validation, and Results

### A. Coherent Combination of L1 C/A and L1C Signals

Before combining, the phases of L1Cd and L1Cp cWFs need to be shifted 90° because of the phase difference. The phase correction of the L1Cd/L1Cp cWF is implemented simply by

$$z'_{\mathrm{L1C}}(t,\tau)=z_{\mathrm{L1C}}(t,\tau)e^{-j\frac{\pi}{2}} \quad (9)$$

where $z'_{\mathrm{L1C}}(t,\tau)$ represents the 1-ms direct/reflected L1Cd/L1Cp cWF after the 90° phase correction.

According to Table I, the minimum received power ratio between L1 C/A, L1Cd, and L1Cp is about 0.44:0.16:0.40. As analyzed in Table II, the power ratio between L1 C/A and L1C signals after the 2.5-MHz bandwidth limiting should be about 1.09:1. With the power ratio between L1Cd and L1Cp normally unchanged, the power ratio between L1 C/A, L1Cd, and L1Cp should be about 0.52:0.14:0.34, which conforms well to that in the measured direct signals, as shown in Table IV. For convenience, the power ratio is deemed as 0.50:0.15:0.35. Assuming that the peak power of the L1 C/A signal is $P$, the powers of L1Cd and L1Cp signals are $0.3P$ and $0.7P$, respectively. To ensure the 1:1 ratio between the L1 C/A component and the L1C component, three components are combined using a weighted strategy

$$z_{\mathrm{com}}(t_0,\tau)=z_{\mathrm{L1CA}}(t_0,\tau)+\sqrt{0.3}z'_{\mathrm{L1Cd}}(t_0,\tau)+\sqrt{0.7}z'_{\mathrm{L1Cp}}(t_0,\tau) \quad (10)$$

where $z_{\mathrm{L1\ C/A}}$, $z_{\mathrm{L1Cd}}$, and $z_{\mathrm{L1Cp}}$ are 1-ms cWFs. Then, $N_I$ combined cWFs are averaged incoherently to generate the power waveform

$$Z_{\mathrm{com}}\left(t+\frac{N_IT_c}{2},\tau\right)=\frac{1}{N_I}\sum_{k=1}^{N_I}|z_{\mathrm{com}}(t+kT_c,\tau)|^2 \quad (11)$$

where $N_I$ is the number of incoherent samples. After processing all CYGNSS raw IF data transmitted by GPS III satellites according to Section II-B2, 23 tracks are generated over the ocean. As mentioned in Section II-B1, only 15 tracks remain with enough SNR. In this article, the average peak SNR over each track is used to evaluate the performance of waveforms as

$$\overline{\mathrm{SNR}}=\frac{1}{N_t}\sum_{i=1}^{N_t}10\lg\frac{Z_{\mathrm{com}}(t_i,\tau_{\max})-P_N(t_i)}{P_N(t_i)} \quad (12)$$

where $N_t$ is the number of incoherent averaged samples in a track, $Z_{\mathrm{com}}(t_i,\tau_{\max})$ denotes the peak power of $Z_{\mathrm{com}}(t_i)$ at the delay of $\tau_{\max}$, and the noise floor $P_N(t_i)$ is calculated by

$$P_N(t_i)=\frac{1}{100}\sum_{j=1}^{100}Z_{\mathrm{com}}(t_i,\tau_j). \quad (13)$$

In this article, the delay of waveforms ranges from −12.248 to 19.585 chips, totaling 500 points with the SP located at the 193rd point of the waveform. According to the ACF width of L1 signals, the first 100 points in the waveform have no signal components.

As analyzed in Section II-A, the peak of the combined power waveform $P_{\mathrm{com}}$ should be 3.84 times compared to that of the L1 C/A component $P_{\mathrm{CA}}$ as

$$P_{\mathrm{com}}(\tau_{\max})=\frac{1}{N_I}\sum|z_{\mathrm{L1CA}}(t,\tau_{\max})+\sqrt{0.3}z'_{\mathrm{L1Cd}}(t,\tau_{\max})+\sqrt{0.7}z'_{\mathrm{L1Cp}}(t,\tau_{\max})|^2\approx 3.84P_{\mathrm{CA}}. \quad (14)$$

The noise power of the correlator output can be calculated by [45], [46]

$$P_N=\frac{N_0}{4T_c}\int_{-B/2}^{B/2}|H(f)|^2G(f)df \quad (15)$$

where $B$ is the receiver bandwidth, $N_0$ is the constant noise power spectrum density (PSD) of the noise, $H(f)$ is the frequency response of the front-end filter, and $G(f)$ is the PSD of the signal. Thus, the theoretical noise power ratio between L1 C/A [BPSK(1)] and L1C [BOC(1, 1)] signals in the CYGNSS data should be

$$\frac{P_N^{\mathrm{L1CA}}}{P_N^{\mathrm{L1C}}}=\frac{\int_{-B/2}^{B/2}|H(f)|^2G_{\mathrm{L1CA}}(f)df}{\int_{-B/2}^{B/2}|H(f)|^2G_{\mathrm{L1C}}(f)df}\approx 1.3 \quad (16)$$

where $P_N^{\mathrm{L1CA}}$ and $P_N^{\mathrm{L1C}}$ are noise powers of L1 C/A and L1C signals, $B$ is equal to 2.5 MHz, and $G_{\mathrm{L1CA}}(f)$ and $G_{\mathrm{L1C}}(f)$ are their PSDs, respectively. The result is close to that calculated from the measured data, which is about 4:3, as shown in Tables IV and V. Both the noise floors of L1 C/A, L1Cd, and L1Cp conform to the zero-mean Gaussian distribution. Supposing the variance of the L1 C/A noise floor as $\sigma^2_{\mathrm{noise}}$, the variance of L1Cd and L1Cp noise floors is about $0.75\sigma^2_{\mathrm{noise}}$ due to the different modulation methods. The weighted summation of them still conforms to a Gaussian distribution

$$N_{\mathrm{com}}=N_{\mathrm{L1CA}}+\sqrt{0.3}N_{\mathrm{L1Cd}}+\sqrt{0.7}N_{\mathrm{L1Cp}}\sim N(0,1.75\sigma^2_{\mathrm{noise}}). \quad (17)$$

The noise power of the combined waveform can be calculated as the expectation

$$P_N^{\mathrm{com}}=E\left[\left(N_{\mathrm{L1CA}}+\sqrt{0.3}N_{\mathrm{L1Cd}}+\sqrt{0.7}N_{\mathrm{L1Cp}}\right)^2\right]=1.75\sigma^2_{\mathrm{noise}}. \quad (18)$$

Based on (14) and (18), the SNR of the combined power waveform should be

$$\mathrm{SNR}_{\mathrm{com}}=10\lg\frac{3.84P_{\mathrm{CA}}}{1.75\sigma^2_{\mathrm{noise}}}. \quad (19)$$

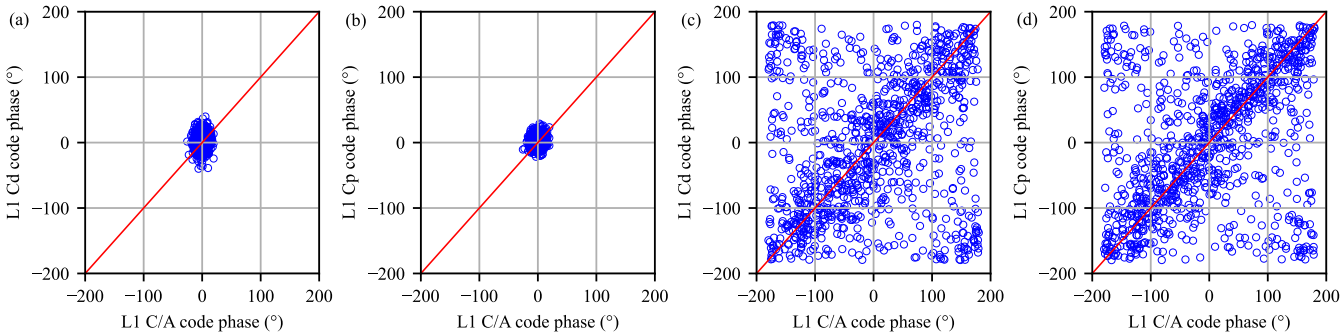


Fig. 5. Phases of direct L1 C/A cWFs compared to those of L1Cd (a) and L1Cp (b) cWFs and those of reflected L1 C/A cWFs versus L1Cd (c) and L1Cp (d) cWFs; 1000 cWFs from 58 to 59 s are selected in Track 11. The phases of direct cWFs are centered at 0 due to closed-loop processing. For reflected cWFs, most samples cluster along with the red 1:1 line after the phase correction. It should be noted that samples on the top left and bottom right of (c) and (d) also have a similar phase, although with a 360° cycle difference.

TABLE IV
POWER RATIO AND AVERAGED SNRS OF FOUR KINDS OF WAVEFORMS OBTAINED FROM DIRECT SIGNALS

| Track ID | Time | FM | GPS PRN | $\overline{SNR}$ (dB) | | | | | Power ratio | |
|---|---|---|---|---|---|---|---|---|---|---|
| | | | | L1 C/A | L1Cd | L1Cp | Combined | $\Delta SNR$ | Signal | Noise |
| 1 | 20200621 | cyg07 | G18 | 15.59 | 11.02 | 14.77 | 18.93 | 3.34 | 0.52:0.14:0.34 | 0.40:0.30:0.30 |
| 2 | 20200912 | cyg08 | G04 | 17.18 | 13.04 | 16.78 | 20.73 | 3.55 | 0.50:0.15:0.35 | 0.39:0.30:0.31 |
| 3 | 20201008 | cyg02 | G23 | 15.86 | 11.16 | 14.96 | 19.14 | 3.28 | 0.53:0.14:0.33 | 0.39:0.31:0.30 |
| 4 | 20201112 | cyg01 | G18 | 14.96 | 10.82 | 14.57 | 18.47 | 3.51 | 0.53:0.14:0.33 | 0.42:0.29:0.29 |
| 5 | 20201112 | cyg01 | G23 | 9.70 | 5.62 | 9.38 | 13.24 | 3.54 | 0.53:0.14:0.33 | 0.42:0.29:0.29 |
| 6 | 20210414 | cyg03 | G23 | 15.72 | 11.50 | 15.30 | 19.20 | 3.48 | 0.53:0.14:0.33 | 0.42:0.29:0.29 |
| 7 | 20210417 | cyg01 | G14 | 15.37 | 11.56 | 15.36 | 19.04 | 3.67 | 0.52:0.14:0.34 | 0.43:0.29:0.28 |
| 8 | 20210417 | cyg02 | G14 | 13.50 | 9.65 | 13.43 | 17.15 | 3.65 | 0.52:0.14:0.34 | 0.43:0.29:0.28 |
| 9 | 20211020 | cyg02 | G04 | 4.94 | 0.56 | 4.29 | 8.42 | 3.48 | 0.50:0.15:0.35 | 0.38:0.31:0.31 |
| 10 | 20220214 | cyg02 | G14 | 13.85 | 9.48 | 13.27 | 17.28 | 3.43 | 0.52:0.14:0.34 | 0.40:0.30:0.30 |
| 11 | 20220303 | cyg01 | G18 | 15.85 | 11.14 | 14.90 | 19.12 | 3.27 | 0.52:0.14:0.34 | 0.39:0.31:0.30 |
| 12 | 20220317 | cyg07 | G14 | 5.97 | 1.66 | 5.43 | 9.45 | 3.48 | 0.52:0.14:0.34 | 0.40:0.30:0.30 |
| 13 | 20220319 | cyg03 | G14 | 16.63 | 12.24 | 16.01 | 20.06 | 3.43 | 0.51:0.15:0.34 | 0.40:0.30:0.30 |
| 14 | 20220422 | cyg01 | G18 | 9.51 | 4.93 | 8.67 | 12.83 | 3.32 | 0.53:0.14:0.33 | 0.40:0.30:0.30 |
| 15 | 20220504 | cyg04 | G23 | 13.16 | 8.79 | 12.58 | 16.58 | 3.42 | 0.53:0.14:0.33 | 0.41:0.30:0.29 |

Therefore, the theoretical SNR improvement ΔSNR can be calculated by

$$\Delta\text{SNR} = \text{SNR}_{\text{com}} - \text{SNR}_{\text{CA}} \approx 3.4 \text{ dB}. \tag{20}$$

### B. Validation Using Direct Signals

To validate the power ratio and phase difference between L1 C/A, L1Cd, and L1Cp components, as well as the SNR improvement, the cWFs of the direct signals are analyzed. As shown in Fig. 5(a) and (b), the phases of the direct L1Cd and L1Cp cWFs are corrected and compared to those of L1 C/A cWFs at the peak of the waveform, in which their phases center at (0, 0) due to the closed-loop processing.

By setting $N_I$ as 1000 (1-s incoherent averaging), the shapes of the L1 C/A and L1C signals, as well as the square of the combined ACFs, are shown in Fig. 6. In addition, a sample including three normalized direct power waveforms is also plotted for comparison. Both L1 C/A and L1C ACFs and normalized waveforms fall within [−1, 1] chips while [−0.5 0.5] chips for the combined ACF and waveform. Except for L1C signals, $\text{ACF}^2$ conforms well to the power waveform of the direct signal, albeit in the presence of some noise. As mentioned earlier, the bandwidth of L1C signals is larger than 2.5 MHz, and some components are filtered.

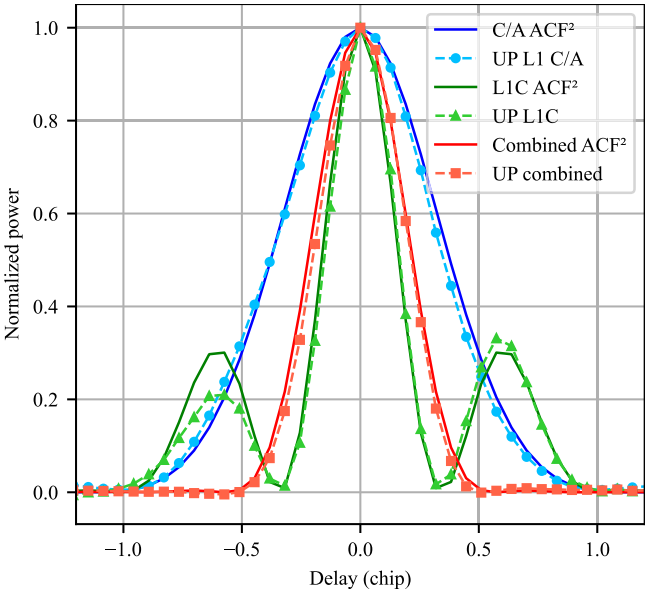


Fig. 6. Comparison between the $\text{ACF}^2$ and the normalized power of received direct GPS L1 C/A, L1C, and combined signals. The bandwidth is limited to 2.5 MHz according to the configuration of CYGNSS receivers using eighth-order low-pass Butterworth filters.

All 15 tracks are processed, and the averaged power ratios and SNRs are shown in Table IV, in which

TABLE V
POWER RATIO AND AVERAGED PEAK SNRS OF FOUR KINDS OF WAVEFORMS USING REFLECTED SIGNALS

| Track ID | Time | FM | GPS PRN | $\overline{SNR}$ (dB) | | | | $\Delta SNR$ | Power ratio | |
|---|---|---|---|---|---|---|---|---|---|---|
| | | | | L1 C/A | L1Cd | L1Cp | Combined | | Signal | Noise |
| 1 | 20200621 | cyg07 | G18 | 0.75 | -6.10 | -2.46 | 2.37 | 1.62 | 0.62:0.12:0.26 | 0.37:0.32:0.31 |
| 2 | 20200912 | cyg08 | G04 | 1.97 | -3.99 | -0.32 | 3.99 | 2.02 | 0.58:0.13:0.29 | 0.38:0.31:0.31 |
| 3 | 20201008 | cyg02 | G23 | 1.17 | -5.02 | -1.54 | 3.02 | 1.85 | 0.61:0.13:0.26 | 0.39:0.31:0.30 |
| 4 | 20201112 | cyg01 | G18 | 0.45 | -5.62 | -2.03 | 2.40 | 1.95 | 0.61:0.12:0.27 | 0.40:0.30:0.30 |
| 5 | 20201112 | cyg01 | G23 | -3.89 | -8.87 | -6.38 | -2.24 | 1.65 | 0.59:0.15:0.26 | 0.40:0.30:0.30 |
| 6 | 20210414 | cyg03 | G23 | -1.00 | -6.68 | -3.01 | 1.11 | 2.11 | 0.60:0.13:0.27 | 0.42:0.29:0.29 |
| 7 | 20210417 | cyg01 | G14 | -3.65 | -7.99 | -4.94 | -1.38 | 2.27 | 0.59:0.14:0.27 | 0.45:0.28:0.27 |
| 8 | 20210417 | cyg02 | G14 | -2.81 | -7.43 | -4.14 | -0.43 | 2.38 | 0.59:0.14:0.27 | 0.44:0.28:0.28 |
| 9 | 20211020 | cyg02 | G04 | -0.51 | -6.06 | -2.69 | 1.21 | 1.72 | 0.59:0.13:0.28 | 0.39:0.30:0.31 |
| 10 | 20220214 | cyg02 | G14 | -5.89 | -9.80 | -8.27 | -4.76 | 1.13 | 0.53:0.20:0.27 | 0.36:0.32:0.32 |
| 11 | 20220303 | cyg01 | G18 | 6.48 | -0.56 | 3.28 | 8.13 | 1.65 | 0.62:0.11:0.27 | 0.36:0.32:0.32 |
| 12 | 20220317 | cyg07 | G14 | 7.15 | 0.97 | 4.92 | 9.32 | 2.17 | 0.59:0.12:0.29 | 0.38:0.31:0.31 |
| 13 | 20220319 | cyg03 | G14 | 4.08 | -2.56 | 1.23 | 5.90 | 1.82 | 0.62:0.11:0.27 | 0.37:0.32:0.31 |
| 14 | 20220422 | cyg01 | G18 | -2.65 | -8.38 | -5.46 | -1.09 | 1.56 | 0.61:0.13:0.26 | 0.39:0.31:0.30 |
| 15 | 20220504 | cyg04 | G23 | -5.89 | -9.41 | -4.22 | -1.67 | 1.56 | 0.57:0.17:0.26 | 0.44:0.28:0.28 |

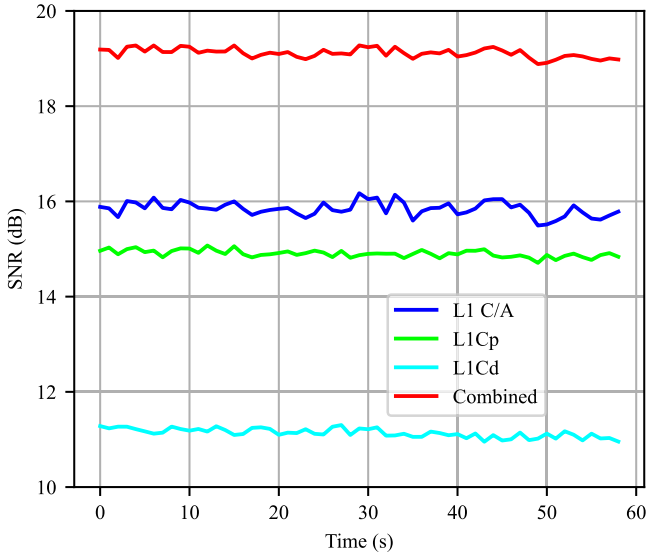


Fig. 7. SNR time series of direct signals in Track 11. The averaged SNRs $\overline{\text{SNR}}$ of combined, L1 C/A, L1Cd, and L1Cp waveforms are, respectively, 19.12, 15.85, 11.14, and 14.90 dB.

$\Delta\text{SNR} = \overline{\text{SNR}_{\text{com}}} - \overline{\text{SNR}_{\text{CA}}}$. The averaged power ratios of received L1 C/A, L1Cd, and L1Cp direct signals and their noise floor are about 0.5:0.15:0.35 and 0.4:0.3:0.3, which conforms well to expected ratios. It ensures that the proposed combining strategy is available. Compared to that of the L1 C/A waveform, the SNR of the combined waveform shows about 3.46-dB improvement computed as (12). This result corroborates the analysis in Section III-A. The SNR time series of direct signals in Track 11 is plotted in Fig. 7. It shows about 3.27-dB stable increments compared to the L1 C/A waveform.

### C. Combination of Reflected Waveforms

The reflected L1 C/A and L1C composite signals can also be combined coherently before the incoherent average. For the ocean scattered signals, there are coherent and incoherent components regarding the sea surface roughness. For the coherent component, the SNR improvement from the combination will be similar to that of the direct signal. However, the incoherent component is dominant in ocean scattering. The scattering mechanism over the ocean and the smaller first isodelay area will degrade the improvement. The theoretical model of the power DDM at each delay $\hat{\tau}$ and Doppler shift $\hat{f}$ is defined as [47]

$$\left\langle P_S(\hat{\tau}, \hat{f}) \right\rangle = P_T G_T \frac{\lambda^2}{(4\pi)^3} \int\int \frac{G_R(\mathbf{r})\sigma_0(\mathbf{r})}{R_T^2(\mathbf{r}) R_R^2(\mathbf{r})} \times \Lambda^2\left[\tau(\mathbf{r}) - \hat{\tau}\right] S^2\left[f(\mathbf{r}) - \hat{f}\right] d\mathbf{r} \tag{21}$$

where $P_T$ is the transmitted GPS signal power, $G_T$ and $G_R$ are transmitter and receiver antenna gains, $R_T$ and $R_R$ are, respectively, the ranges from the ocean surface point to the transmitter and receiver, $\lambda$ is the signal carrier wavelength, $\sigma_0$ is the bistatic radar cross section (BRCS), and $\Lambda$ and $S$ are ACF and sinc function, whose combination is called the Woodward ambiguity function (WAF).

As discussed previously, the combined waveform is concentrated within a smaller delay range and has a sharper shape. From the model in (21), the following aspects should be noted.

1) On the one hand, the spatial resolution (defined by the pulse-limited footprint size) of the combined waveform observation is expected to be improved.
2) On the other hand, the effective area (footprint size) of the sea surface is reduced by a factor ~2, which will reduce the total power of the reflected signal.
3) Moreover, according to the relationship between the Doppler shift and theoretical maximum coherence time in [48], a narrower first isodelay ellipse leads to a smaller Doppler shift separation and a larger maximum coherence interval, which can allow longer coherent integration time of the combined waveform.

These aspects will be analyzed in detail and validated by using these 15 tracks of data.

*1) Spatial Resolution:* The "horseshoe" shape DDM is centered on the SP, which is the power summation from each grid around the SP in the glistening zone. Fig. 8 shows the footprint corresponding to a DDM, which is divided by multiple isodelay ellipses and iso-Doppler lines. The reflected

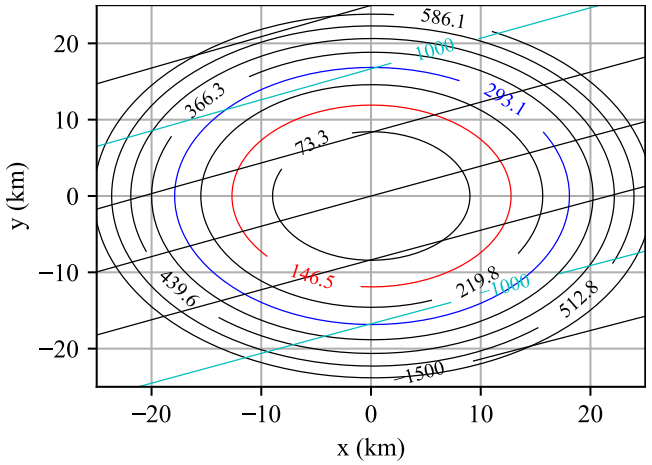


Fig. 8. Distribution of the delay and Doppler shift of the reflected signal over the surface (incidence angle $i = 22.29°$, azimuth angle $\alpha = 118.10°$, and CYGNSS receiver altitude $H = 539\,231$ m). The blue and red ellipses are the first isodelay ellipses of L1 C/A and combined signals, respectively.

power from each DDM bin is mapped into the scattered power from their corresponding intersection grids. For the GPS L1 C/A scattered power at the SP, it includes the scattered signals from the region with the delay of [0, 1] chips (blue isodelay ellipse in Fig. 8). For the combined signal, the width of the ACF is half of the L1 C/A's ACF, and the surface region contributing to the SP of the DDM is within the delay of [0, 0.5] C/A code chips. Without considering the Doppler shift, the spatial resolutions of the L1 C/A and combined DDM are about 17.5 and 12.5 km in diameter, respectively, with area resolution improved by 50%.

*2) SNR:* Following the same coherent combination strategy, the cWFs of the reflected signal from L1 C/A, L1Cd, and L1Cp have been also processed. Similar to the direct signals combination, the phases of the reflected L1Cd and L1Cp cWFs are corrected and compared to those of L1 C/A cWFs at the peak of the waveform in Fig. 5(c) and (d). It can be seen that their phases are, in general, consistent with each other, however, with a relatively larger dispersion than those of the direct signals.

The power waveforms generated from L1 C/A, L1Cd, L1Cp, and their combination are compared in Fig. 9 (top). The peak power and noise floor of the combined waveform are about 2.68 and 1.90 times higher than that of the L1 C/A waveform, corresponding to an SNR improvement of 1.66 dB. To compare the shape of waveforms, they are normalized after removing the noise floor as Fig. 9 (bottom). It is shown that the combined waveform is with a steeper leading edge slope (LES). According to (26), the ranging standard deviation (STD) is partly determined by the ranging sensitivity $S_r$, which is defined as the normalized slope of the waveform. Therefore, the increasing LES of the combined waveform will contribute to increasing $S_r$ and reducing the ranging STD, which implies better altimetry performance.

It is noted that the SNR improvement of the reflected signal using the combination of L1 C/A and L1C components is not as high as that of the direct signal (i.e., ∼2 versus ∼3 dB). This is due to the smaller effective scatter area of the SP bin for

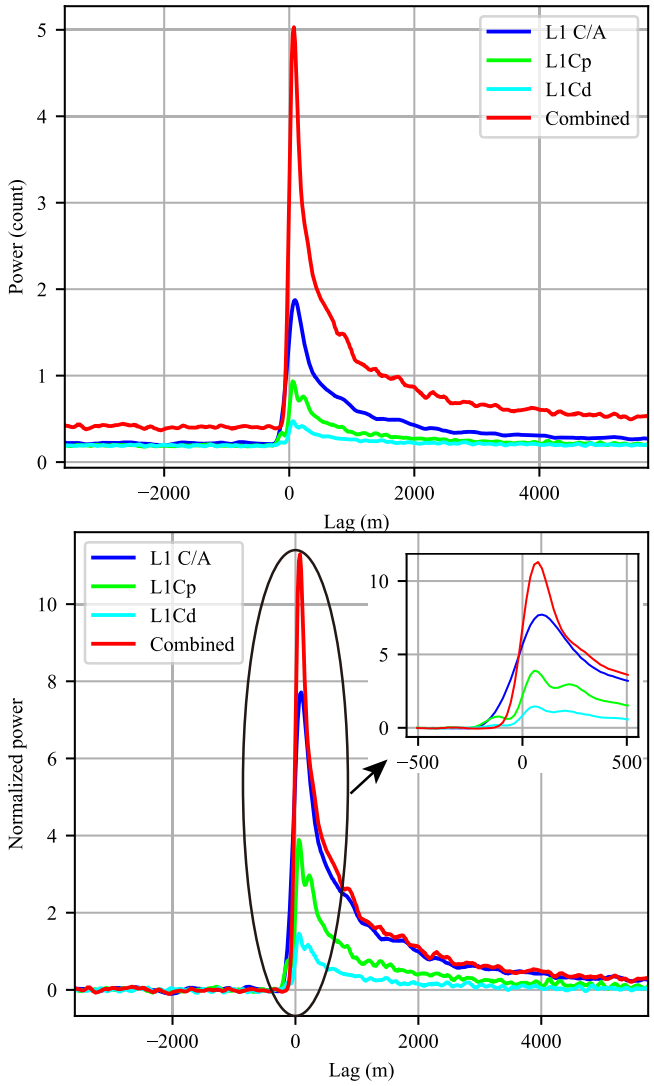


Fig. 9. 1-s incoherently averaged reflected L1 C/A, L1Cd, L1Cp, and combined power waveforms (top) and their normalized power waveforms (bottom) from Track 11. The noise floor of each waveform in the bottom plot is calculated as (13) and has been removed.

the combined waveform (narrower ACF). To compare the peak power between L1 C/A and combined waveforms, the simulation described in the Appendix is performed. The simulated peak power of the normalized combined waveform is about $2.26P$–$2.96P$ under different incidence angles, azimuths, and wind speeds. The noise floor of the combined reflected signal remains at about $1.75\sigma^2_{\text{noise}}$. The theoretical SNR improvement of reflected signals can be calculated by

$$\begin{aligned}\Delta\text{SNR}_r &= \text{SNR}^r_{\text{com}} - \text{SNR}^r_{\text{CA}} \\ &= 10\lg\frac{P^r_{\text{com}}}{1.75\sigma^2_{\text{noise}}}\frac{\sigma^2_{\text{noise}}}{P^r_{\text{CA}}} \in [1.11\text{ dB}, 2.28\text{ dB}] \quad (22)\end{aligned}$$

where $P^r_{\text{com}}$ and $P^r_{\text{CA}}$ denote the peak power of combined and L1 C/A waveforms, respectively. Based on this simulating method, the simulated L1 C/A and combined waveforms are also generated for 15 tracks. Then, the ratio between the peak power of simulated L1 C/A and combined waveforms is compared to that of measured waveforms. As shown in Fig. 10, the simulations slightly underestimate the power ratio

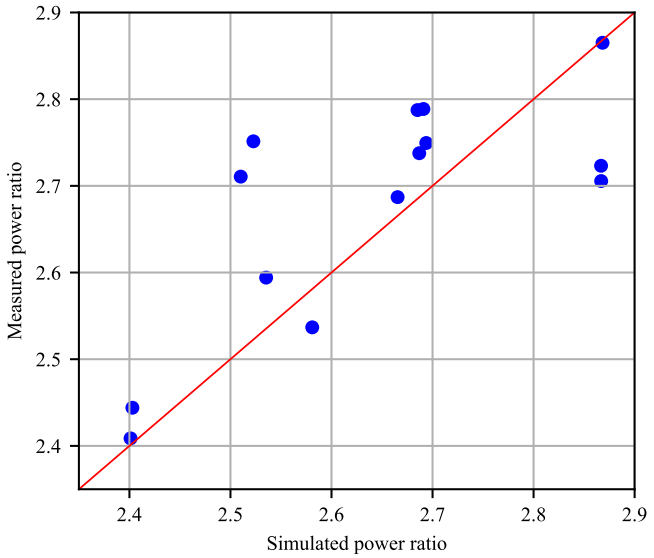


Fig. 10. Comparison between the simulated and measured power ratio for all 15 tracks. The median power ratio for each track is calculated.

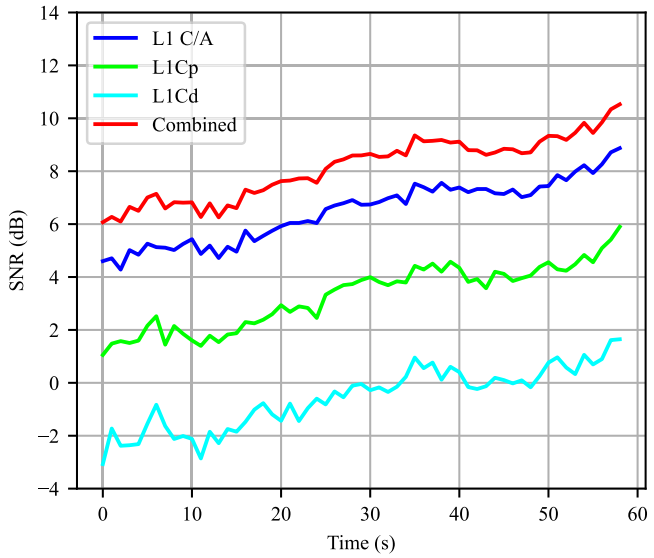


Fig. 11. SNR time series of reflected signals. The averaged SNRs $\overline{\text{SNR}}$ of combined, L1 C/A, L1Cd, and L1Cp waveforms are, respectively, 8.12, 6.48, −0.56, and 3.28 dB.

while overall conforming well to the measured one. It proves that the simulation is conservative yet effective and consistent with the measurements.

As shown in Table V, the SNRs of the combined waveforms show a 1.93-dB improvement on average computed as (12). The range of SNR increments is almost consistent with the simulation result, from 1.13 to 2.38 dB. To observe the performance on continuous samples, the SNR time series of Track 11 is plotted in Fig. 11. It shows approximately 1.65-dB stable increments compared to the L1 C/A waveform. It is also noted that the SNR of the L1C signals (i.e., L1Cd or L1Cp) is lower than that of the GPS L1 C/A signal (e.g., 7.0 and 3.2 dB lower than that of L1 C/A in Track 11), which implies a degraded performance in geophysical applications. Therefore, we only compare the ranging and scatterometry performance between the L1 C/A and combined waveforms in Section IV.

*3) Coherent Integration Time:* The smaller footprint size of the reflected L1 combined signal (as shown in Fig. 8) implies a narrower Doppler bandwidth of the reflected signal within its footprint, which makes it possible to use longer coherent integration time for the combined signal than the L1 C/A code signal. This assumption can be validated by applying different coherent integration intervals of 1/2/3/4/5 ms to the cWFs, along with a 10-s incoherent averaging time.

Table VI shows the SNRs of the reflected C/A code signal and L1 combination using different coherent intervals, which indicates that longer coherent intervals can reduce thermal noise and enhance the SNR. In most of the tracks, the SNR is the highest when using the 5-ms coherent interval. Fig. 12 (left) shows the averaged SNR at the SP of all tracks at different coherent intervals for L1 C/A and combined waveforms, which clearly shows that the SNR can be improved by increasing the coherent interval. For the combined waveforms, the averaged SNR using the 5-ms coherent interval is improved by 2.13 dB compared to that using 1 ms, while it is about 1.54 dB for the L1 C/A waveform. For convenience, the averaged SNR increment at different coherent intervals between two waveforms is shown in Fig. 12 (right). For the combined waveform, the SNR is always larger, and $\Delta$SNR tends to be saturated when the coherent interval reaches 4 ms.

## IV. Preliminary Performance Validation in Geophysical Applications

Due to the higher SNR and steeper LES, the geophysical retrieval performances using the L1 C/A and L1C combined waveform are expected to be improved. In this section, we take ocean altimetry and wind speed retrieval as examples to demonstrate the performance improvement brought by the proposed processing approach.

### A. Ocean Altimetry

*1) Waveform Retracking:* GNSS-R ocean altimetry performance relies on the LES of the measured power waveform. The altimetry retrieval applied to the L1 C/A and L1C combination can be referenced to [19]. The half retracking approach is exploited in this work, in which the delay where the power is a given fraction of the peak power is taken on the leading edge of the waveform as the retracking point. Typically, the fraction is set as about 0.5. However, as for GNSS-R waveforms, we select 0.75 according to Cardellach et al. [49].

After obtaining the incoherent L1 C/A and L1 combined waveforms, the noise floor is removed from the power waveform, and a cubic interpolation is applied to obtain a high-resolution waveform with a 100 times shorter delay interval. Then, the delay where the power is $0.75Z(t, \tau_{\max})$ is found on the high-resolution waveform. An example of the L1 C/A waveform using the half retracker is shown in Fig. 13, and its range measurement is 3.18 m.

TABLE VI

AVERAGED SNRS AT THE SP OF L1 C/A AND COMBINED WAVEFORMS USING DIFFERENT COHERENT INTERVALS AND THE AVERAGED PEAK POWER RATIO BETWEEN L1 C/A, L1CD, AND L1CP COMPONENTS

| Track ID | Time | FM | SNR (dB) | | | | | | | | | |
|---|---|---|---|---|---|---|---|---|---|---|---|---|
| | | | 1 ms | | 2 ms | | 3 ms | | 4 ms | | 5 ms | |
| | | | C/A | Combined | C/A | Combined | C/A | Combined | C/A | Combined | C/A | Combined |
| 1 | 20200621 | cyg07 | 0.94 | 2.59 | 1.23 | 3.07 | 1.19 | 3.01 | 1.46 | 3.30 | 1.42 | 3.32 |
| | | | $P_{C/A} : P_{Cd} : P_{Cp} = 0.61 : 0.12 : 0.27$ | | | | | | | | | |
| 2 | 20200912 | cyg08 | 2.22 | 4.27 | 2.51 | 4.75 | 2.50 | 4.77 | 2.62 | 4.96 | 2.73 | 5.04 |
| | | | $P_{C/A} : P_{Cd} : P_{Cp} = 0.58 : 0.29 : 0.13$ | | | | | | | | | |
| 3 | 20201008 | cyg02 | 1.26 | 3.11 | 1.61 | 3.61 | 1.72 | 3.70 | 1.80 | 3.81 | 1.80 | 3.83 |
| | | | $P_{C/A} : P_{Cd} : P_{Cp} = 0.61 : 0.12 : 0.27$ | | | | | | | | | |
| 4 | 20201112 | cyg01 | 0.40 | 2.36 | 0.74 | 2.80 | 0.50 | 2.61 | 0.96 | 3.07 | 1.03 | 3.07 |
| | | | $P_{C/A} : P_{Cd} : P_{Cp} = 0.62 : 0.11 : 0.27$ | | | | | | | | | |
| 5 | 20201112 | cyg01 | -3.91 | -2.24 | -3.55 | -1.56 | -3.50 | -1.48 | -3.47 | -1.38 | -3.28 | -1.29 |
| | | | $P_{C/A} : P_{Cd} : P_{Cp} = 0.61 : 0.12 : 0.27$ | | | | | | | | | |
| 6 | 20210414 | cyg03 | -0.91 | 1.22 | 0.02 | 2.47 | -0.85 | 1.53 | 0.22 | 2.75 | 0.39 | 2.86 |
| | | | $P_{C/A} : P_{Cd} : P_{Cp} = 0.60 : 0.12 : 0.28$ | | | | | | | | | |
| 7 | 20210417 | cyg01 | -3.86 | -1.54 | -3.45 | -1.00 | -3.41 | -0.78 | -3.27 | -0.74 | -3.29 | -0.66 |
| | | | $P_{C/A} : P_{Cd} : P_{Cp} = 0.59 : 0.13 : 0.28$ | | | | | | | | | |
| 8 | 20210417 | cyg02 | -3.06 | -0.65 | -2.80 | -0.27 | -2.66 | -0.13 | -2.72 | -0.10 | -2.45 | -0.03 |
| | | | $P_{C/A} : P_{Cd} : P_{Cp} = 0.60 : 0.12 : 0.28$ | | | | | | | | | |
| 9 | 20211020 | cyg02 | -0.02 | 1.80 | 0.87 | 3.00 | 1.12 | 3.27 | 1.36 | 3.48 | 1.33 | 3.46 |
| | | | $P_{C/A} : P_{Cd} : P_{Cp} = 0.58 : 0.12 : 0.30$ | | | | | | | | | |
| 10 | 20220214 | cyg02 | -5.80 | -4.59 | -4.72 | -3.13 | -4.45 | -2.87 | -4.38 | -2.80 | -4.28 | -2.85 |
| | | | $P_{C/A} : P_{Cd} : P_{Cp} = 0.59 : 0.14 : 0.27$ | | | | | | | | | |
| 11 | 20220303 | cyg01 | 6.20 | 7.85 | 6.47 | 8.29 | 6.58 | 8.45 | 6.67 | 8.52 | 6.70 | 8.57 |
| | | | $P_{C/A} : P_{Cd} : P_{Cp} = 0.60 : 0.12 : 0.28$ | | | | | | | | | |
| 12 | 20220317 | cyg07 | 7.46 | 9.56 | 9.24 | 11.50 | 9.90 | 12.20 | 10.24 | 12.55 | 10.41 | 12.74 |
| | | | $P_{C/A} : P_{Cd} : P_{Cp} = 0.59 : 0.12 : 0.29$ | | | | | | | | | |
| 13 | 20220319 | cyg03 | 4.00 | 5.83 | 4.28 | 6.27 | 4.40 | 6.42 | 4.41 | 6.44 | 4.51 | 6.48 |
| | | | $P_{C/A} : P_{Cd} : P_{Cp} = 0.60 : 0.12 : 0.28$ | | | | | | | | | |
| 14 | 20220422 | cyg01 | -2.53 | -0.96 | -2.04 | -0.14 | -1.92 | -0.03 | -1.88 | 0.02 | -1.86 | 0.12 |
| | | | $P_{C/A} : P_{Cd} : P_{Cp} = 0.61 : 0.12 : 0.27$ | | | | | | | | | |
| 15 | 20220504 | cyg04 | -5.96 | -4.18 | -4.89 | -2.66 | -4.62 | -2.26 | -4.55 | -2.28 | -4.65 | -2.25 |
| | | | $P_{C/A} : P_{Cd} : P_{Cp} = 0.60 : 0.13 : 0.27$ | | | | | | | | | |

In this article, the range precision is defined as the STD of the delay residual from the model

$$\sigma_\rho^{\text{obs}} = \sqrt{\left\langle |\delta\rho_{\text{res}} - \langle \delta\rho_{\text{res}} \rangle|^2 \right\rangle} \tag{23}$$

where $\delta\rho_{\text{res}} = \rho_{\text{obs}} - \rho_{\text{model}}$. The model delay $\rho_{\text{model}}$ for each track is estimated from the Technical University of Denmark (DTU) mean sea surface (MSS) model. Then, the height residual can be calculated according to the geometric relationship

$$\delta h = -\frac{\delta\rho_{\text{res}}}{2\cos i} \tag{24}$$

where $i$ is the incidence angle. The altimetric precision can be calculated after the conversion from range to height measurements.

The median absolute deviation (MAD) is also chosen as a robust metric in case outliers exist. The MAD of range measurements $\text{MAD}_\rho^{\text{obs}}$ is calculated by

$$\text{MAD}_\rho^{\text{obs}} = M[|\delta\rho_{\text{res}} - M(\delta\rho_{\text{res}})|] \tag{25}$$

where $M$ is the median. The MAD of the height $\text{MAD}_h^{\text{obs}}$ can also be calculated by (24) and (25).

As proposed in [50], the ranging precision $\sigma_\rho$ can be predicted theoretically as

$$\sigma_\rho = \frac{1}{S_r(\tau_{\text{rtk}})\sqrt{N_I}} \times \left[\frac{1}{R(\tau_{\text{rtk}})} + \frac{1}{\text{PN}(\tau_{\text{rtk}})}\right] \tag{26}$$

where $\tau_{\text{rtk}}$ is the delay of the retracking point, $S_r$ is the altimetry sensitivity computed from the modeled waveform by $S_r = Z'(\tau_{\text{rtk}})/Z(\tau_{\text{rtk}})$, which is directly correlated to LES, $R$ is the effectiveness of incoherent average, and $\text{PN}(\tau_{\text{rtk}})$ is defined as

$$\text{PN}(\tau_{\text{rtk}}) = 0.75\frac{P - P_N}{P_N} = 0.75 \times 10^{\frac{SNR}{10}}. \tag{27}$$

For simplification, an empirical expression for CYGNSS L1 C/A ranging precision is approximated as [19]

$$\sigma_\rho = 3.28 \times \left[1.08 + \frac{1}{\text{PN}(\tau_{\text{rtk}})}\right]. \tag{28}$$

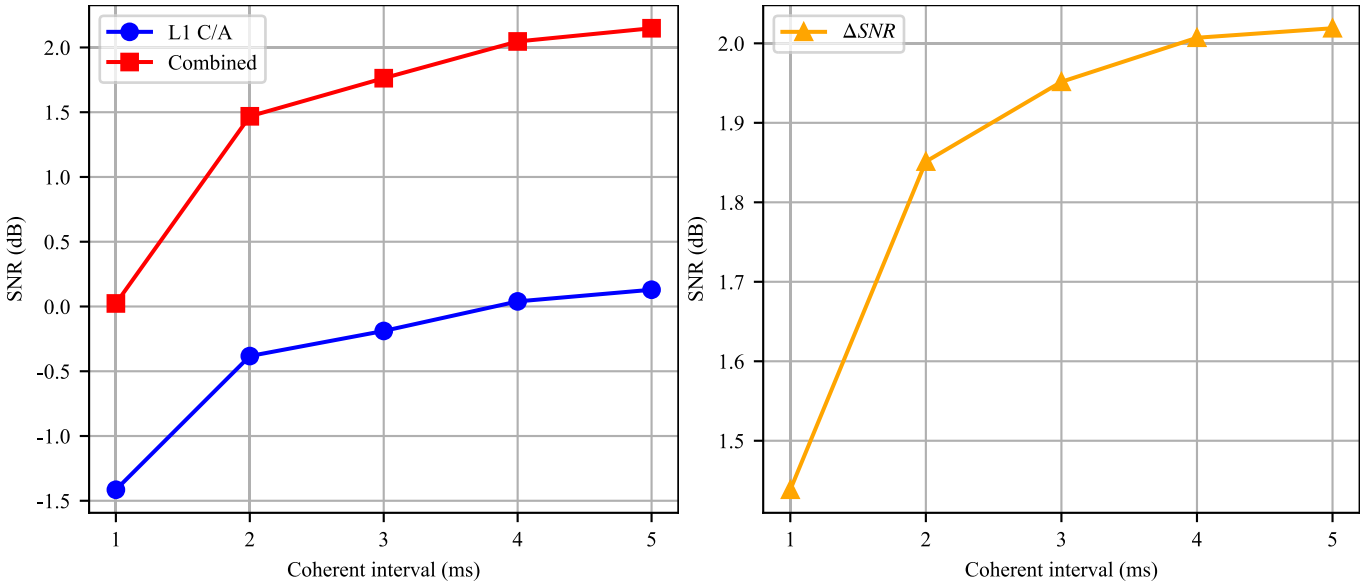


Fig. 12. Averaged SNR at the SP of the waveform for all 15 tracks using different coherent intervals (left) and the averaged ΔSNR between the combined and L1 C/A waveforms versus coherent intervals (right). It can be found that the improvement saturates at 5 ms. With the increasing coherent integration time, the signal bandwidth decreases until the signal component is also filtered out except for noise. Thus, the SNR of signals cannot be improved anymore although increasing the coherent interval.

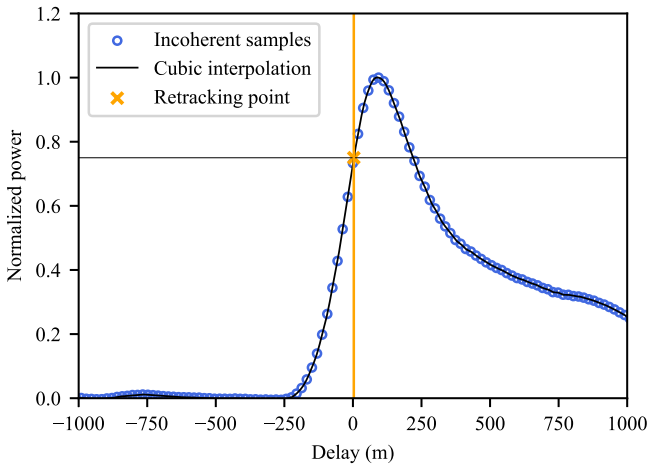


Fig. 13. Example of half retracking. The incoherent L1 C/A waveform after removing the noise floor calculated by (13) is normalized by the peak power. The delay of the half retracking point is 3.18 m.

As calculated in Section III-C2, the combined waveform exhibits an improved SNR. According to (26), both the altimetry sensitivity $S_r$ and SNR of the combined waveform increase. Hence, the theoretical range precision $\sigma_\rho$ should be improved. A fitting of the empirical relationship between $\sigma_\rho$ and SNR for the combined waveform will be conducted.

*2) Altimetry Performance of the Combined Waveform:* The half retracking method is implemented on the selected tracks with the results shown in Table VII. It can be found that the ranging precision varies from 2.74 to 6.53 m with 1-Hz code delay measurements from the combined waveforms, which is more stable compared to L1 C/A from 4.57 to 15.61 m. The ranging STD improves by 35.3%–61.6%, and the MAD improves by 22.4%–64.4%. Furthermore, the STD of height measurements is between 1.53 and 7.77 m. The ranging STDs obtained from L1 C/A and combined waveforms for all tracks are presented as a function of the SNR in Fig. 14. It shows great agreement between the model prediction in (28) and the realistic STD for L1 C/A delay measurements. A model function for the combined delay measurements is also generated based on the least square principle as

$$\sigma_\rho^{\text{com}} = 2.03 \times [1.25 + 1/\text{PN}(\tau_{\text{rtk}})]. \tag{29}$$

As discussed above and shown in Fig. 9, the LES of combined ACF is steeper than the L1 C/A ACF, which contributes to a better ranging sensitivity [by a factor of about 1.6 according to (28) and (29)]. The input of the two model curves is converted from PN to SNR($\tau_{\max}$) for the comparison. It demonstrates that the delay measurements from combined waveforms are more stable than those from L1 C/A waveforms, which benefits from the narrower ACF and SNR improvement.

The ranging precision of two tracks, Tracks 8 and 11, is evaluated in detail. Fig. 15 shows the time series of delay residuals from both the combined and L1 C/A waveforms, corresponding to the low and high SNR situation. It is notable that the delay measurements from the combined waveforms show smaller fluctuations, especially when the SNR of the L1 C/A waveform is low, as shown in Fig. 15 (top). According to the empirical relationship between the ranging STD and SNR for L1 C/A and combined waveforms, the STD improvement is more evident when the SNR is low so that the fluctuations are smaller. It is noted that in this article, we focus on analyzing the STD of the delay measurements to obtain the altimetric precision of the proposed combined waveform. Therefore, the retracking point of the combined waveform is selected by using the same half factor as that of the L1 C/A waveform,

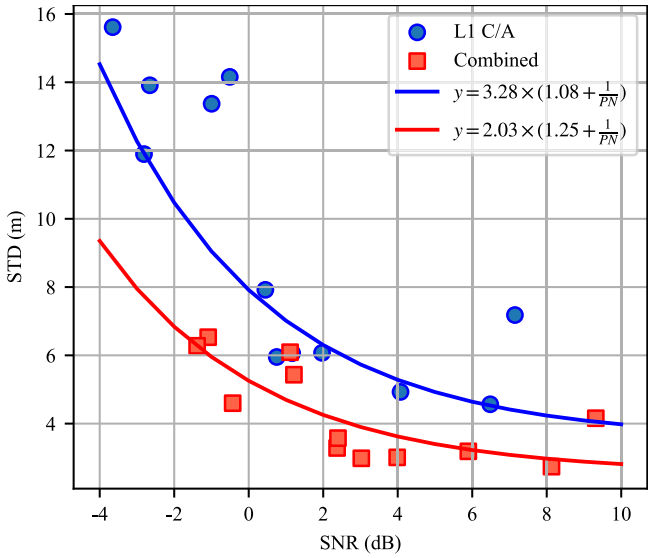


Fig. 14. Ranging precision of delay measurements from reflected L1 C/A and combined waveforms versus the SNR. The model curve of L1 C/A is presented as (28), while the model curve of the combined situation is fit using the least square principle.

which can be further optimized to improve the altimetry accuracy.

To intuitively validate the altimetric results, the height retrievals from L1 C/A and combined waveforms in Track 11 and Track 13 are compared to the DTU18 MSS model, as shown in Fig. 16. It can be found that the height retrievals calculated using combined observations are distributed closer to the model height with a smaller fluctuation in both tracks. The RMSEs of combined height retrievals compared to DTU 18 MSS in Track 11 and Track 13 are 1.53 and 2.38 m, respectively, improved by 40.0% and 35.3% compared to those of L1 C/A height retrievals. It also proves that the coherent combined waveform shows better altimetric precision.

### *B. Ocean Wind Speed Retrieval*

To assess its performance on wind speed retrieval, the SNR measurements are utilized and calibrated along each track. Generally, $\sigma_0$ is used to retrieve ocean wind speed, which is calculated by unwrapping the power DDM. The waveform generated in this article is in counts, which can be calibrated to the power DDM with necessary parameters, such as the instrument gain. For simplification, we directly use the SNR of the waveform in counts and remove the influence of the receiver gain and geometry to obtain an approximate BRCS $\sigma_p$ according to (21), where the joint influence of the gain and geometry can be defined as range corrected gain (RCG). In the cWF products, the positions and velocities of GPS transmitters and CYGNSS receivers are calculated and provided, as outlined in Section II-B2. Then, the azimuth and elevation angles of signals reflected from the SP are calculated in the CYGNSS body frame. The antenna pattern is determined by them to calculate the linearized receiver gain $G_{Rl}$. Finally, the linearized SNR is normalized by RCG

$$\sigma_p = \frac{10^{\frac{\mathrm{SNR}}{10}}}{\mathrm{RCG}} = \frac{10^{\frac{\mathrm{SNR}}{10}} R_T^2 R_R^2}{G_{Rl}} \times 10^{-27}. \tag{30}$$

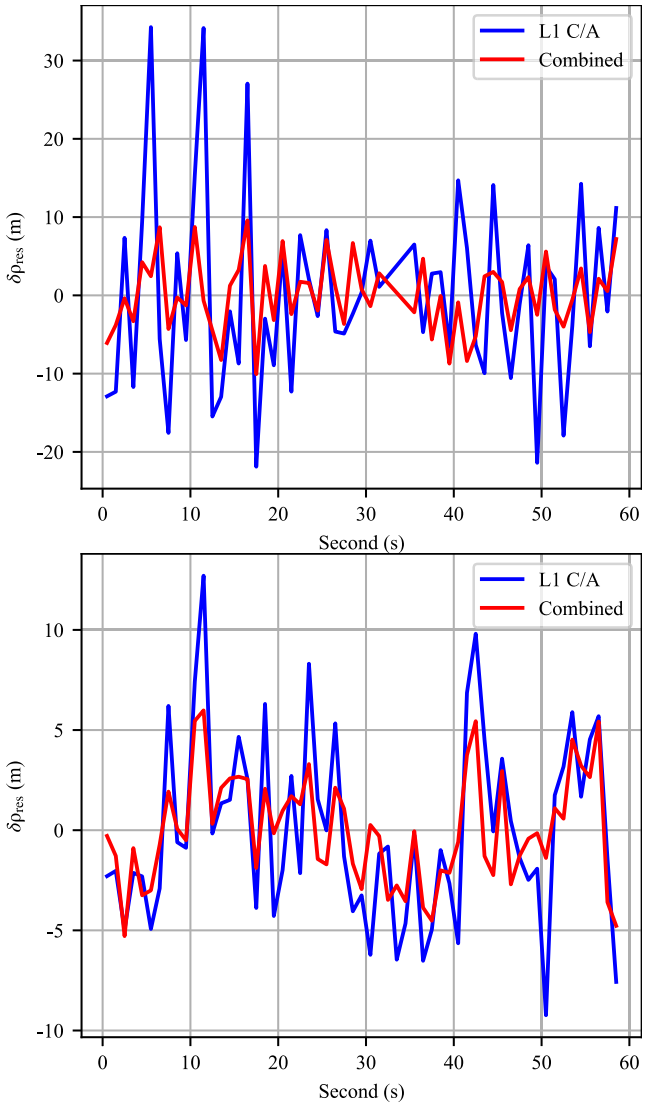


Fig. 15. Time series of delay measurements in Track 8 (top) and Track 11 (bottom). In Track 8 (top), the measurements at 32–34 s are flagged as blackbody samples, and they are discarded. The ranging measurements from the combined waveform show a lower STD.

To compare the performance of $\sigma_p$ derived from L1 C/A and combined waveforms on wind speed retrieval, the Pearson correlation coefficient $R$ is computed as

$$R = \frac{\sum_{i=1}^{N_t}[\sigma_p(i) - \overline{\sigma_p}(i)][u_{10}(i) - \overline{u_{10}}(i)]}{\sqrt{\sum_{i=1}^{N_t}[\sigma_p(i) - \overline{\sigma_p}(i)]^2}\sqrt{\sum_{i=1}^{N_t}[u_{10}(i) - \overline{u_{10}}(i)]^2}} \tag{31}$$

where $u_{10}$ is the matched European Center for Medium-Range Weather Forecasts (ECMWF) ERA5 wind speed, and $N_t$ is the number of samples in a track.

The quality control is performed through three filtering criteria, including the following.

1) The incidence angle is larger than 60° (Track 9, Track 12, and Track 14).
2) There are samples with abnormally high $\sigma_p$ of L1 C/A signals in the tracking (Track 6 and Track 13).
3) The relationship between $\sigma_p$ of L1 C/A signals and wind speed is abnormally positive (Track 3 and Track 11).

TABLE VII
STD AND MAD OF RANGE AND HEIGHT MEASUREMENTS FROM L1 C/A AND COMBINED WAVEFORMS

| Track ID | Time | FM | $\sigma_\rho^{CA}$ (m) | $\sigma_\rho^{com}$ (m) | $MAD_\rho^{CA}$ (m) | $MAD_\rho^{com}$ (m) | $\sigma_h^{CA}$ (m) | $\sigma_h^{com}$ (m) | $MAD_h^{CA}$ (m) | $MAD_h^{com}$ (m) |
|---|---|---|---|---|---|---|---|---|---|---|
| 1 | 20200621 | cyg07 | 5.95 | 3.29 | 4.80 | 2.82 | 3.63 | 2.01 | 2.95 | 1.72 |
| 2 | 20200912 | cyg08 | 6.07 | 3.01 | 6.14 | 2.51 | 3.97 | 1.97 | 4.01 | 1.64 |
| 3 | 20201008 | cyg02 | 6.06 | 2.98 | 6.09 | 3.60 | 3.78 | 1.86 | 3.80 | 2.25 |
| 4 | 20201112 | cyg01 | 7.92 | 3.57 | 6.44 | 3.60 | 4.44 | 2.00 | 3.59 | 2.01 |
| 6 | 20210414 | cyg03 | 13.37 | 6.09 | 9.33 | 5.04 | 9.39 | 4.24 | 6.46 | 3.49 |
| 7 | 20210417 | cyg01 | 15.61 | 6.28 | 16.70 | 5.94 | 10.10 | 4.06 | 10.80 | 3.84 |
| 8 | 20210417 | cyg02 | 11.90 | 4.60 | 12.00 | 4.67 | 6.83 | 2.64 | 6.89 | 2.68 |
| 9 | 20211020 | cyg02 | 14.16 | 5.43 | 12.23 | 5.68 | 20.20 | 7.77 | 17.49 | 8.06 |
| 11 | 20220303 | cyg01 | 4.57 | 2.74 | 4.45 | 2.94 | 2.55 | 1.53 | 2.49 | 1.64 |
| 12 | 20220317 | cyg07 | 7.18 | 4.16 | 8.80 | 4.76 | 11.45 | 6.63 | 14.32 | 7.57 |
| 13 | 20220319 | cyg03 | 4.93 | 3.19 | 4.09 | 3.17 | 2.86 | 1.85 | 2.38 | 1.85 |
| 14 | 20220422 | cyg01 | 13.91 | 6.53 | 14.26 | 5.90 | 15.06 | 7.05 | 15.37 | 6.26 |

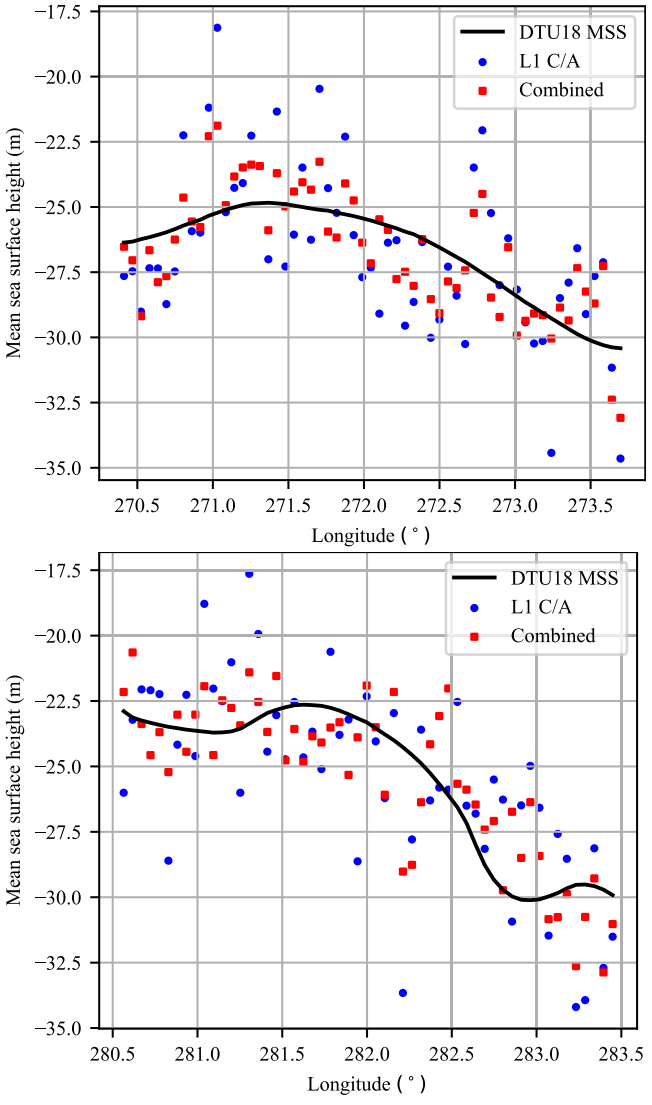


Fig. 16. Two examples of height retrieved using L1 C/A and combined waveforms in Track 11 (left) and Track 13 (right). They are chosen due to the more obvious change of height compared to other tracks. Heights retrieved using combined waveforms are more robust and clustered around the DTU 18 MSS model.

After the quality control, there are eight tracks left. The averaged SNR and $R$ are calculated, along with wind speed shown in Table VIII. It should be noted that when calculating the SNR in this analysis, the peak power of the waveform is replaced by the averaged power within $[\tau_{max} - 2, \tau_{max} + 2]$. Although the averaged SNR is slightly different from that in Table V, there is still a 1.74-dB improvement compared to the L1 C/A waveform. After converting the SNR to $\sigma_p$, the correlation coefficient of all tracks is calculated, as shown in Table VIII. Overall, $R_{com}$ is more negative than $R_{CA}$, with improved anticorrelation by 2.4%–46%. Due to the decreasing sensitivity of GNSS-R observable with increasing wind speed, the absolute value of the correlation coefficient for L1 C/A measurements is smaller than 0.52 for Tracks 5, 7, and 8, tracks of higher wind speed. The combined measurements always show a higher anticorrelation with wind speed, particularly for high winds, improved by about 26.3% on average.

The relationship between $\sigma_p$ and the wind speed of all tracks is plotted in Fig. 17. $\sigma_p$ calculated using combined measurements and correlation coefficients, as shown in Table VIII, is always larger than that using L1 C/A measurements. L1 C/A waveforms show low SNRs at high winds, which ruins the wind retrieval performance. Moreover, $\sigma_p$ is less sensitive at high winds, and a small disturbance can lead to a large wind speed retrieval error. After the coherent combination, the SNR of combined waveforms is improved so that the STD of wind speed retrieval decreases. Therefore, the combined observable is more robust at high winds, thereby improving its performance at high winds.

This preliminary validation demonstrates the potential of the proposed coherent combined waveform for wind speed retrieval. The linearized SNR after normalization shows a higher correlation to wind speed compared to the traditional L1 C/A measurements. However, the power calibration is not well performed, and the influence of GPS effective isotropic radiated power (EIRP) is not removed from $\sigma_p$. In addition, the limited samples within a track hinder the generation of a robust geophysical model function for wind speed retrieval. Nevertheless, it is proven that the proposed coherent combining method can improve wind speed retrieval performance. In future works, the calibration algorithm should be developed for the new GPS III L1C and combined signals. Further validation of its performance can be conducted by collecting more samples and implementing quality control.

TABLE VIII

AVERAGED SNR AND PEARSON CORRELATION COEFFICIENT $R$ BETWEEN $\sigma_p$ CALCULATED BY L1 C/A AND COMBINED WAVEFORMS AND WIND SPEED

| Track ID | Time | FM | GPS PRN | $\overline{SNR_{\text{CA}}}$ (dB) | $\overline{SNR_{\text{com}}}$ (dB) | $R_{\text{CA}}$ | $R_{\text{com}}$ | $\overline{u_{10}}$ (m/s) |
|---|---|---|---|---|---|---|---|---|
| 1 | 20200621 | cyg07 | G18 | 0.66 | 2.15 | -0.551 | -0.566 | 7.51 |
| 2 | 20200912 | cyg08 | G04 | 1.88 | 3.77 | -0.696 | -0.763 | 5.03 |
| 4 | 20201112 | cyg01 | G18 | -0.08 | 1.75 | -0.584 | -0.706 | 6.21 |
| 5 | 20201112 | cyg01 | G23 | -4.05 | -2.50 | -0.276 | -0.402 | 18.16 |
| 7 | 20210417 | cyg01 | G14 | -3.75 | -1.61 | -0.513 | -0.664 | 19.94 |
| 8 | 20210417 | cyg02 | G14 | -2.92 | -0.68 | -0.356 | -0.370 | 19.90 |
| 10 | 20220214 | cyg02 | G14 | -4.82 | -3.68 | -0.845 | -0.865 | 2.94 |
| 15 | 20220504 | cyg04 | G23 | -6.02 | -4.42 | -0.718 | -0.835 | 4.77 |

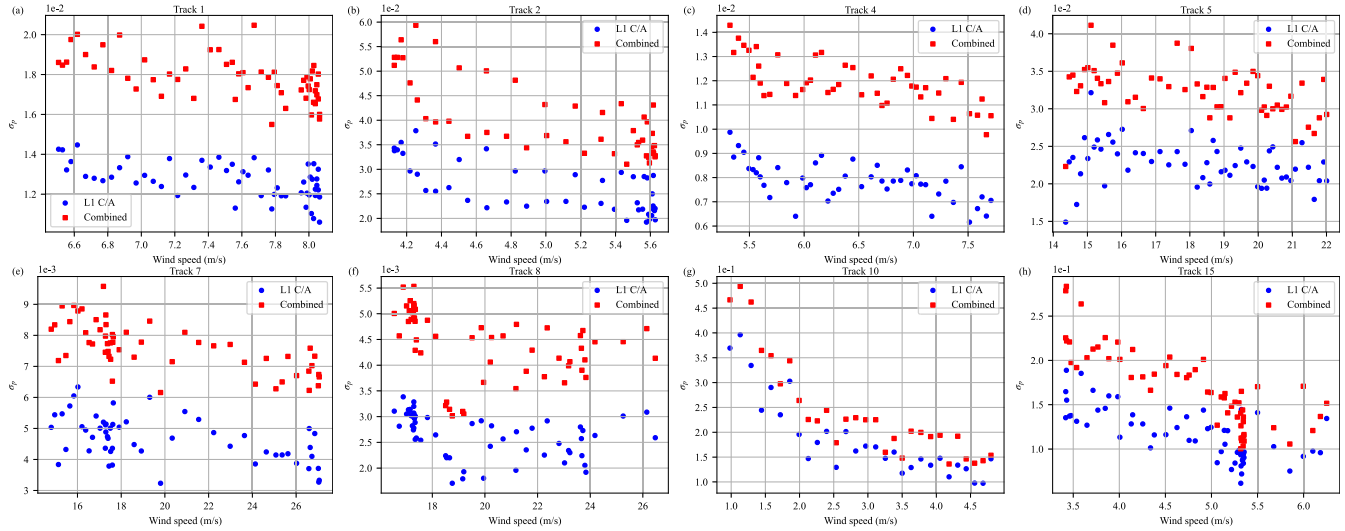


Fig. 17. Comparison between $\sigma_p$ and wind speed for L1 C/A and combined measurements in (a) Track 1, (b) Track 2, (c) Track 4, (d) Track 5, (e) Track 7, (f) Track 8, (g) Track 10, and (h) Track 15. $\sigma_p$ from the combined waveform is always larger than that from the L1 C/A waveform.

## V. CONCLUSION

Large-scale ocean altimetry is difficult for iGNSS-R due to the limitation of the antenna gain although multiple types of GNSS signals can be applied and the altimetric precision is higher. As for cGNSS-R, the ocean altimetry performance can be further improved using modernized GNSS signals. The utilization of modernized GNSS signals and the development of future spaceborne GNSS-R payloads are crucial for overcoming the limitations posed by commonly used L1 C/A reflected signals. In this article, a coherently combined waveform is proposed by incorporating GPS III L1 C/A, L1Cd, and L1Cp reflected signals based on their ACF characteristics. The resulting waveform has a better spatial resolution due to the narrower ACF and a higher SNR resulting from a higher transmitted power compared to the traditional L1 C/A waveform. The increased SNR contributes to improving the performance of ocean altimetry and wind speed retrieval. In addition, the higher spatial resolution can lead to a more accurate retrieval and further monitoring of smaller scale details of the ocean surface. Different tracks of CYGNSS raw IF data are processed, from which GPS III L1 C/A and L1C 1-ms cWFs are generated for each track. Despite the CYGNSS receiver bandwidth hindering the collection of one of the L1C components, the results of the combined waveform with the BOC(1, 1) modulations of L1C show improved performances. When using 1-s incoherent time, the SNR of the combined waveform is improved by 1.13–2.38 dB. More SNR improvement for the combined waveform can be obtained using longer coherent intervals compared to the L1 C/A waveform. The performance of GNSS-R geophysical applications using the combined waveforms has been analyzed preliminarily. Initial altimetric tests show that the STD and MAD of ranging measurements decrease by 35.3%–61.6% and 22.4%–64.4%, respectively. In addition, the correlation coefficient between $\sigma_p$ and wind speed improves by 46% at most under high winds. These improvements in geophysical applications can be foreseen due to the narrower ACF and improved SNR of the L1 C/A and L1C combination.

The new coherent combination method for spaceborne cGNSS-R stands out with a salient SNR improvement, which is an exploration using the modernized GPS III reflected signals. Other than ocean altimetry, DDM observables, such as LES and normalized BRCS (NBRCS), can be extracted from the combined DDM for ocean wind speed retrieval, significant wave height retrieval, and so on. Due to a few samples (less than 1 min) included in a raw IF file, the large-scale performance is difficult to validate. However, it is possible that the proposed combining method can be directly implemented in the DDM instrument (DDMI), and the combined waveform or DDM can be transmitted through the downlink channel for further analysis and applications. In addition, HydroGNSS to be launched in 2024 will generate raw IF data at least on

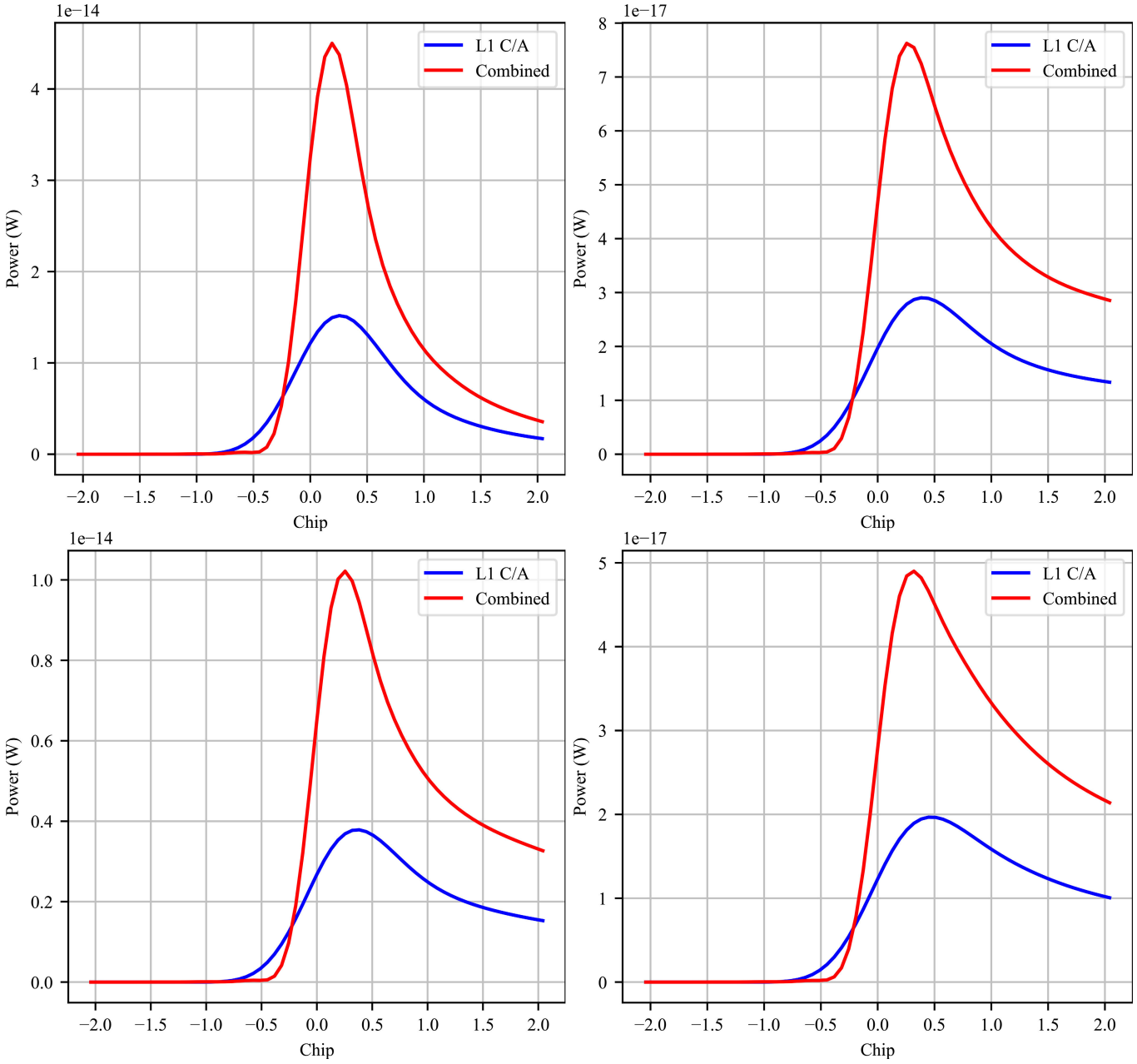


Fig. 18. Simulated L1 C/A and corresponding combined waveforms with different incidence angles $i$, azimuth angles $\alpha$, and wind speeds $u$: $i = 11.96°, \alpha = 271.92°$, and $u = 0.03$ m/s (top left); $i = 35.30°, \alpha = 136.56°$, and $u = 7.96$ m/s (top right); $i = 33.29°, \alpha = 244.51°$, and $u = 0.52$ m/s (bottom left); and $i = 60.79°, \alpha = 35.27°$, and $u = 14.20$ m/s (bottom right). The power ratios are 2.96, 2.63, 2.70, and 2.49, respectively.

a daily basis. With these new data, we believe that its ocean altimetric and wind speed retrieval performance can be further validated. With the development of the GNSS-R technique, more kinds of GNSS-R reflected signals, such as Galileo E1 [19] and BeiDou-3 B1C [51], are studied and show improved performance in ocean altimetry and wind speed retrieval. In the next generation of the GNSS-R payload, multiple types of reflected GNSS signals can be processed and explored to improve the GNSS-R sensing ability, which may expand the new potential applications.

## Appendix
## Simulation of L1 C/A and Combined Waveforms

The 2-D convolution simulating method in [52] is applied to generate simulated L1 C/A and combined waveforms. The metadata, such as the positions and velocities of the transmitter and receiver, the position of the SP, the signal incidence angle, the receiver antenna gain, and the EIRP of the GPS transmitter antenna, are extracted from the CYGNSS L1 V2.1 data files [43]. Each sample is bilinearly interpolated in space and linearly interpolated in time with the ECMWF ERA5 reanalysis 10-m wind speed products [53].

The ACFs of L1 C/A and combined waveforms with the 2.5-MHz bandwidth are applied, as shown in Figs. 2 (left) and 3. The delay resolution is about 0.064 chips (16.0362-MHz sampling rate), which is consistent with the cWFs generated in this article. The delay waveform ranges from −2.048 to 2.048 chips. The Doppler resolution is 500 Hz with the range from −2500 to 2500 Hz. In this article, only the delay waveform at the 0 Doppler bin is analyzed. When

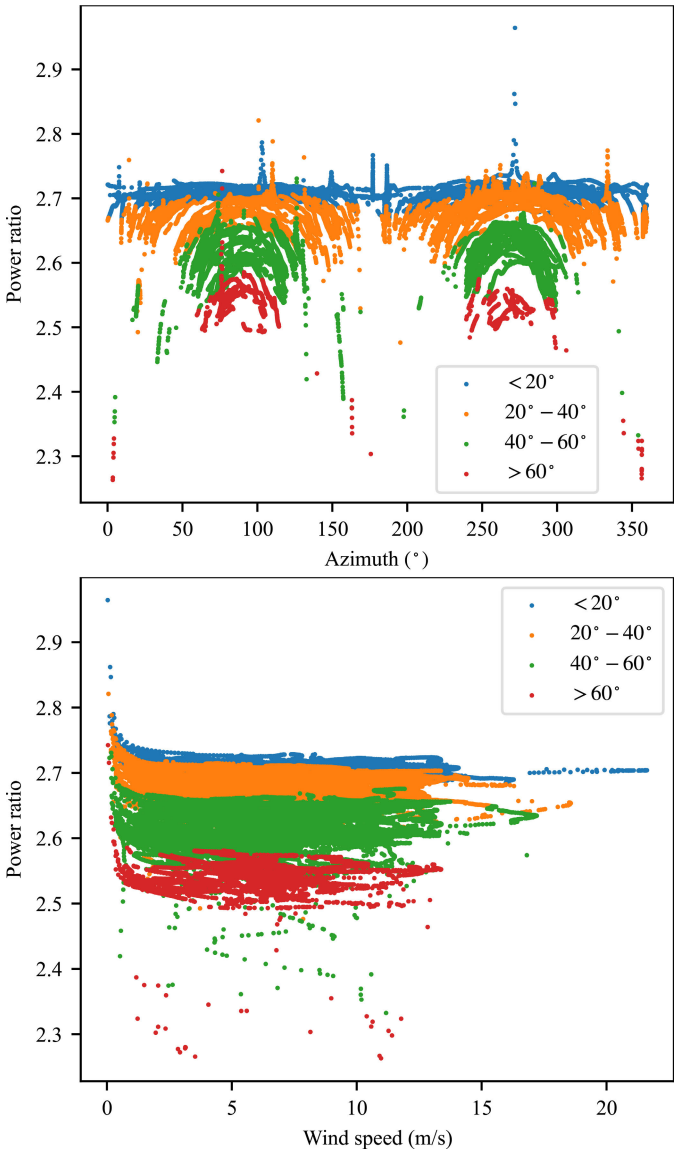


Fig. 19. Power ratio versus the azimuth (top) and wind speed (bottom) with different incidence angles.

calculating the power grid around the SP, the grid resolution is 200 m. According to Fernando Marchan-Hernandez et al. [52], (21) can be rewritten as a 2-D convolution

$$P_S(\hat{\tau}, \hat{f}) = G(\tau, f) * * \chi^2(\hat{\tau}, \hat{f}) \tag{32}$$

where $G(\tau, f)$ is the power grid of L1 C/A reflected signals without scattering and can be computed as

$$G(\tau, f) = \frac{\lambda^2 P_t G_t}{(4\pi)^3} \int\int \frac{G_R(\mathbf{r})\sigma_0[\mathbf{r}, \mathbf{u}(\mathbf{r})]}{R_T^2(\mathbf{r}) R_R^2(\mathbf{r})} \times \delta[\tau - \tau(\mathbf{r})]\delta[f - f(\mathbf{r})]d\mathbf{r} \tag{33}$$

where $\sigma_0[\mathbf{r}, \mathbf{u}(\mathbf{r})]$ is the BRCS of the facet $\mathbf{r}$, computed by the Katzberg wind/wave model [54] for the wind vector $\mathbf{u}(\mathbf{r})$, $\delta(\cdot)$ is the Dirac delta function, and $\chi^2(\hat{\tau}, \hat{f})$ is the WAF in (21).

Fig. 18 shows some examples of L1 C/A and combined waveforms at different incidence angles, azimuths, and wind speeds. The peak power ratio between the simulated combined and L1 C/A waveforms ranges from 2.26 to 2.96, which is lower than that of the direct signals. It can be found that with the increase in the incidence angle, the power ratio decreases. According to Clarizia et al. [55], the ellipses tend to be wider for higher incidence angles, resulting in a larger shrunk scattered area for the combined signals. In addition, the power ratio appears to be less influenced by wind speed. To further investigate the relationship between the power ratio and incidence angle, azimuth, and wind speed, we selected the measurements collected by the "cyg01" CYGNSS satellite on February 17, 2019. Bad samples are filtered out by setting the "quality_flags" equal to 0. The samples are then divided into different ranges of incidence angle: [0, 20°], [20°, 40°], [40°, 60°], and [60°, 80°]. The peak power ratio versus the azimuth and wind speed in different ranges of the incidence angle is plotted in Fig. 19. It can be found that with the increase in the incidence angle, the power ratio decreases as analyzed above. Furthermore, the power ratio shows a periodic change with the azimuth because 0°–180° and 180°–360° denote the signals received from starboard and port antennas, respectively, as shown in Fig. 19 (top). When the azimuth is equal to 90° or 270°, the power ratio reaches the maximum. As for the combined waveform, the shrunk area depends on the cross field of isodelay ellipses and iso-Doppler lines. Referring to Fig. 8, when the iso-Doppler line is parallel to the semimajor axis of isodelay ellipses, the shrunk area is minimum, and the lost power is also minimum. As the azimuth changes, the shrunk area increases and reaches maximum until the azimuth is equal to 0 or 180° (180° or 360°).

In this section, we simulate the combined waveform based on 2.5-MHz ACFs and CYGNSS L1 metadata. It is found that the incidence angle and azimuth are the two main factors determining the power ratio between the combined and L1 C/A waveforms. The improvement of the peak power is about 2.26–2.96 times, which is lower than that of the direct signal. As analyzed above, it is caused by signal scattering and the narrower ACF. Nonetheless, the combined waveform shows a narrower width and larger power, which is consistent with the theoretical analysis.

## Acknowledgment

The authors are grateful to the Cyclone Global Navigation Satellite System (CYGNSS) public raw IF data and L1 V2.1 data from the NASA Physical Oceanography Distributed Active Archive Center (PO.DAAC; https://doi.org/10.5067/CYGNS-L1RIF, https://doi.org/10.5067/CYGNS-L1X21) and the European Center for Medium-Range Weather Forecasts (ECMWF) reanalysis wind products (available at doi: 10.24381/cds.adbb2d47). Weiqiang Li and Estel Cardellach are the CYGNSS mission's extended science team members.

## References

[1] V. U. Zavorotny, S. Gleason, E. Cardellach, and A. Camps, "Tutorial on remote sensing using GNSS bistatic radar of opportunity," *IEEE Geosci. Remote Sens. Mag.*, vol. 2, no. 4, pp. 8–45, Dec. 2014.

[2] S. Jin, E. Cardellach, and F. Xie, *GNSS Remote Sensing*, vol. 16. Cham, Switzerland: Springer, 2014.

[3] A. Rius and E. Cardellach, "Reflectometry," in *Springer Handbook of Global Navigation Satellite Systems*. Cham, Switzerland: Springer, 2017, pp. 1163–1186.

[4] H. Carreno-Luengo et al., "The IEEE-SA working group on spaceborne GNSS-R: Scene study," *IEEE Access*, vol. 9, pp. 89906–89933, 2021.

[5] R. Balasubramaniam and C. Ruf, "Characterization of rain impact on L-band GNSS-R ocean surface measurements," *Remote Sens. Environ.*, vol. 239, Mar. 2020, Art. no. 111607.

[6] C. D. Hall and R. A. Cordey, "Multistatic scatterometry," in *Proc. Int. Geosci. Remote Sens. Symp., Remote Sens. Moving Toward 21st Century*, vol. 1, Sep. 1988, pp. 561–562.

[7] M. Martín-Neira, "A passive reflectometry and interferometry system (PARIS): Application to ocean altimetry," *ESA J.*, vol. 17, no. 4, pp. 331–355, Dec. 1993.

[8] J. L. Garrison, S. J. Katzberg, and M. I. Hill, "Effect of sea roughness on bistatically scattered range coded signals from the global positioning system," *Geophys. Res. Lett.*, vol. 25, no. 13, pp. 2257–2260, Jul. 1998.

[9] M. Martin-Neira, M. Caparrini, J. Font-Rossello, S. Lannelongue, and C. S. Vallmitjana, "The Paris concept: An experimental demonstration of sea surface altimetry using GPS reflected signals," *IEEE Trans. Geosci. Remote Sens.*, vol. 39, no. 1, pp. 142–150, Jan. 2001.

[10] E. Cardellach, F. Fabra, O. Nogués-Correig, S. Oliveras, S. Ribó, and A. Rius, "GNSS-R ground-based and airborne campaigns for ocean, land, ice, and snow techniques: Application to the GOLD-RTR data sets," *Radio Sci.*, vol. 46, no. 6, pp. 1–16, Dec. 2011.

[11] M. Unwin, S. Gleason, and M. Brennan, "The space GPS reflectometry experiment on the U.K. disaster monitoring constellation satellite," in *Proc. 16th Int. Tech. Meeting Satellite Division Inst. Navigat.*, 2003, pp. 2656–2663.

[12] S. D'Addio, M. Martin-Neira, F. Martín, H. Park, and A. Camps, "GNSS-R altimeter performance: Analysis of cramer-rao lower bounds," in *Proc. Workshop Reflectometry GNSS Other Signals Opportunity (GNSS+R)*, Oct. 2012, pp. 1–4.

[13] M. P. Clarizia, C. P. Gommenginger, S. T. Gleason, M. A. Srokosz, C. Galdi, and M. Di Bisceglie, "Analysis of GNSS-R Delay-Doppler maps from the U.K.-DMC satellite over the ocean," *Geophys. Res. Lett.*, vol. 36, no. 2, pp. 1–16, Jan. 2009.

[14] S. Gleason, M. Adjrad, and M. Unwin, "Sensing ocean, ice and land reflected signals from space: Results from the U.K.-DMC GPS reflectometry experiment," in *Proc. 18th Int. Tech. Meeting Satell. Division Inst. Navigat.*, 2005, pp. 1679–1685.

[15] M. Unwin, P. Jales, J. Tye, C. Gommenginger, G. Foti, and J. Rosello, "Spaceborne GNSS-reflectometry on TechDemoSat-1: Early mission operations and exploitation," *IEEE J. Sel. Topics Appl. Earth Observ. Remote Sens.*, vol. 9, no. 10, pp. 4525–4539, Oct. 2016.

[16] C. Ruf, S. Gleason, A. Ridley, R. Rose, and J. Scherrer, "The NASA CYGNSS mission: Overview and status update," in *Proc. IEEE Int. Geosci. Remote Sens. Symp. (IGARSS)*, Jul. 2017, pp. 2641–2643.

[17] J. Mashburn et al., "A comparison of waveform model re-tracking methods using data from CYGNSS," in *Proc. IEEE Int. Geosci. Remote Sens. Symp.*, Jul. 2018, pp. 4289–4292.

[18] E. Cardellach et al., "First precise spaceborne sea surface altimetry with GNSS reflected signals," *IEEE J. Sel. Topics Appl. Earth Observ. Remote Sens.*, vol. 13, pp. 102–112, 2020.

[19] W. Li, E. Cardellach, F. Fabra, S. Ribó, and A. Rius, "Assessment of spaceborne GNSS-R ocean altimetry performance using CYGNSS mission raw data," *IEEE Trans. Geosci. Remote Sens.*, vol. 58, no. 1, pp. 238–250, Jan. 2020.

[20] B. Downs, A. J. Kettner, B. D. Chapman, G. R. Brakenridge, A. J. O'Brien, and C. Zuffada, "Assessing the relative performance of GNSS-R flood extent observations: Case study in south Sudan," *IEEE Trans. Geosci. Remote Sens.*, vol. 61, 2023, Art. no. 4201213.

[21] J. Tye, P. Jales, M. Unwin, and C. Underwood, "The first application of stare processing to retrieve mean square slope using the SGR-ReSI GNSS-R experiment on TDS-1," *IEEE J. Sel. Topics Appl. Earth Observ. Remote Sens.*, vol. 9, no. 10, pp. 4669–4677, Oct. 2016.

[22] J. Crespo, D. Posselt, and S. Asharaf, "CYGNSS surface heat flux product development," *Remote Sens.*, vol. 11, no. 19, p. 2294, Oct. 2019.

[23] C. C. Chew and E. E. Small, "Soil moisture sensing using spaceborne GNSS reflections: Comparison of CYGNSS reflectivity to SMAP soil moisture," *Geophys. Res. Lett.*, vol. 45, no. 9, pp. 4049–4057, May 2018.

[24] C. Chew et al., "SMAP radar receiver measures land surface freeze/thaw state through capture of forward-scattered L-band signals," *Remote Sens. Environ.*, vol. 198, pp. 333–344, Sep. 2017.

[25] K. Rautiainen, D. Comite, J. Cohen, E. Cardellach, M. Unwin, and N. Pierdicca, "Freeze–Thaw detection over high-latitude regions by means of GNSS-R data," *IEEE Trans. Geosci. Remote Sens.*, vol. 60, 2022, Art. no. 4302713.

[26] H. Carreno-Luengo and C. S. Ruf, "Mapping freezing and thawing surface state periods with the CYGNSS based F/T seasonal threshold algorithm," *IEEE J. Sel. Topics Appl. Earth Observ. Remote Sens.*, vol. 15, no. 1, pp. 9943–9952, Jun. 2022.

[27] M. C. Evans and C. S. Ruf, "Toward the detection and imaging of ocean microplastics with a spaceborne radar," *IEEE Trans. Geosci. Remote Sens.*, vol. 60, 2022, Art. no. 4202709.

[28] C. Jing, X. Niu, C. Duan, F. Lu, G. Di, and X. Yang, "Sea surface wind speed retrieval from the first Chinese GNSS-R mission: Technique and preliminary results," *Remote Sens.*, vol. 11, no. 24, p. 3013, Dec. 2019.

[29] F. Huang et al., "Characterization and calibration of spaceborne GNSS-R observations over the ocean from different BeiDou satellite types," *IEEE Trans. Geosci. Remote Sens.*, vol. 60, 2022, Art. no. 5804511.

[30] P. Jales et al., "The new spire GNSS-R satellite missions and products," in *Image Signal Processing Remote Sensing*, vol. 11533. Bellingham, WA, USA: SPIE, 2020, p. 1153316.

[31] A. Camps et al., "FSSCat: The federated satellite systems 3Cat mission: Demonstrating the capabilities of CubeSats to monitor essential climate variables of the water cycle [Instruments and missions]," *IEEE Geosci. Remote Sens. Mag.*, vol. 10, no. 4, pp. 260–269, Dec. 2022.

[32] M. J. Unwin et al., "An introduction to the HydroGNSS GNSS reflectometry remote sensing mission," *IEEE J. Sel. Topics Appl. Earth Observ. Remote Sens.*, vol. 14, no. 1, pp. 6987–6999, Aug. 2021, doi: 10.1109/JSTARS.2021.3089550.

[33] P. Steigenberger, S. Thoelert, and O. Montenbruck, "GPS III vespucci: Results of half a year in orbit," *Adv. Space Res.*, vol. 66, no. 12, pp. 2773–2785, Dec. 2020.

[34] R. T. Anthony, *NAVSTAR GPS Space Segment/User Segment L1C Interfaces*, document IS-GPS-800J, Navstar GPS Directorate, Vela Way, CA, USA, 2022.

[35] P. Jales, "Spaceborne receiver design for scatterometric GNSS reflectometry," Ph.D. dissertation, Surrey Space Centre, Univ. Surrey, Guildford, England, 2012.

[36] H.-Y. Wang and J.-C. Juang, "Retrieval of ocean surface wind speed using reflected BPSK/BOC signals," *Remote Sens.*, vol. 12, no. 17, p. 2698, Aug. 2020.

[37] F. Fabra, E. Cardellach, W. Li, and A. Rius, "WAVPY: A GNSS-R open source software library for data analysis and simulation," in *Proc. IEEE Int. Geosci. Remote Sens. Symp. (IGARSS)*, Jul. 2017, pp. 4125–4128.

[38] F. Saïd, Z. Jelenak, J. Park, and P. S. Chang, "The NOAA track-wise wind retrieval algorithm and product assessment for CyGNSS," *IEEE Trans. Geosci. Remote Sens.*, vol. 60, 2022, Art. no. 4202524.

[39] W. Li, E. Cardellach, S. Ribó, S. Oliveras, and A. Rius, "Exploration of multi-mission spaceborne GNSS-R raw IF data sets: Processing, data products and potential applications," *Remote Sens.*, vol. 14, no. 6, p. 1344, Mar. 2022.

[40] R. T. Anthony, *Navstar GPS Space Segment/navigation User Segment Interfaces*, document IS-GPS-200N, Navstar GPS Directorate, Vela Way, CA, USA, 2022.

[41] CYGNSS. (2020). *CYGNSS Level 1 Raw Intermediate Frequency Data Record*. [Online]. Available: https://podaac.jpl.nasa.gov/dataset/CYGNSS_L1_RAW_IF

[42] O. Montenbruck et al., "The multi-GNSS experiment (MGEX) of the international GNSS service (IGS)—Achievements, prospects and challenges," *Adv. Space Res.*, vol. 59, no. 7, pp. 1671–1697, Apr. 2017.

[43] CYGNSS. (2017). *Cygnss Level 1 Science Data Record Version 2.1*. [Online]. Available: https://podaac.jpl.nasa.gov/dataset/CYGNSS_L1_V2.1

[44] E. Kaplan and C. J. Hegarty, *Understanding GPS/GNSS: Principles and Applications*. Norwood, MA, USA: Artech House, 2017.

[45] J. W. Betz, "Binary offset carrier modulations for radionavigation," *Navigation*, vol. 48, no. 4, pp. 227–246, Dec. 2001.

[46] O. Julien, "Design of Galileo L1F receiver tracking loops," Ph.D. dissertation, Dept. Geomatics Eng., Univ. Calgary, Calgary, Canada, 2005.

[47] V. U. Zavorotny and A. G. Voronovich, "Scattering of GPS signals from the ocean with wind remote sensing application," *IEEE Trans. Geosci. Remote Sens.*, vol. 38, no. 2, pp. 951–964, Mar. 2000.

[48] G. A. Hajj and C. Zuffada, "Theoretical description of a bistatic system for ocean altimetry using the GPS signal," *Radio Sci.*, vol. 38, no. 5, pp. 1–10, Oct. 2003.

[49] E. Cardellach et al., "Consolidating the precision of interferometric GNSS-R ocean altimetry using airborne experimental data," *IEEE Trans. Geosci. Remote Sens.*, vol. 52, no. 8, pp. 4992–5004, Aug. 2014.

[50] W. Li, A. Rius, F. Fabra, E. Cardellach, S. Ribó, and M. Martín-Neira, "Revisiting the GNSS-R waveform statistics and its impact on altimetric retrievals," *IEEE Trans. Geosci. Remote Sens.*, vol. 56, no. 5, pp. 2854–2871, May 2018.

[51] W. Li, E. Cardellach, S. Ribó, A. Rius, and B. Zhou, "First spaceborne demonstration of BeiDou-3 signals for GNSS reflectometry from CYGNSS constellation," *Chin. J. Aeronaut.*, vol. 34, no. 9, pp. 1–10, Sep. 2021, doi: 10.1016/j.cja.2020.11.016.

[52] J. Fernando Marchan-Hernandez, A. Camps, N. Rodriguez-Alvarez, E. Valencia, X. Bosch-Lluis, and I. Ramos-Perez, "An efficient algorithm to the simulation of Delay-Doppler maps of reflected global navigation satellite system signals," *IEEE Trans. Geosci. Remote Sens.*, vol. 47, no. 8, pp. 2733–2740, Aug. 2009.

[53] R. Owens and T. Hewson. (2018). *ECMWF Forecast User Guide*. [Online]. Available: https://www.ecmwf.int/node/16559

[54] S. J. Katzberg, O. Torres, and G. Ganoe, "Calibration of reflected GPS for tropical storm wind speed retrievals," *Geophys. Res. Lett.*, vol. 33, no. L18602, Sep. 2006.

[55] M. P. Clarizia, V. Zavorotny, D. Mc Kague, and C. Ruf, "Level 2 wind speed retrieval algorithm theoretical basis document," Univ. Michigan, Ann Arbor, MI, USA, CYGNSS Project, UM Doc. 148-0138, Rev 7, 2021.

**Hao Du** (Graduate Student Member, IEEE) received the B.E. degree in engineering of surveying and mapping and the M.E. degree in control science and engineering from Wuhan University, Wuhan, Hubei, China, in 2019 and 2022, respectively. He is currently pursuing the Ph.D. degree in marine sciences with the Earth Observation Research Group, Institute of Space Sciences (ICE), Spanish National Research Council (CSIC), Institut d'Estudis Espacials de Catalunya (IEEC), University of Barcelona, Barcelona, Spain.

His research interests include global navigation satellite system (GNSS) reflectometry techniques, ocean wind/wave, and machine learning.

**Yang Nan** received the B.S. and M.S. degrees in geomatics from Chang'an University, Xi'an, China, in 2012 and 2017, respectively, and the Ph.D. degree in geodesy and surveying engineering from the GNSS Research Center, Wuhan University, Wuhan, China, in 2022.

From 2019 to 2020, he studied at the Earth Observation Research Group, Institute of Space Sciences (ICE), Spanish National Research Council (CSIC), Institutd'Estudis Espacials de Catalunya (IEEC), Barcelona, Spain. Since July 2022, he has been an Assistant Researcher with the School of Marine Science and Technology, Tianjin University, Tianjin, China. He has been involved in spaceborne global navigation satellite system reflectometry (GNSS-R) to the Earth observation.

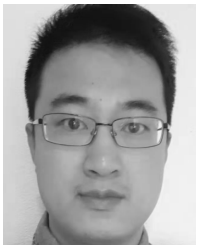

**Weiqiang Li** (Senior Member, IEEE) received the B.S. degree in electronic engineering and the Ph.D. degree in communication and information systems from Beihang University, Beijing, China, in 2004 and 2012, respectively. His Ph.D. thesis was on the signal processing methods and instrumentation of the Earth-reflected global navigation satellite system (GNSS) signal for remote sensing purposes.

Since 2014, he has been with the Earth Observation Research Group, Institute of Space Sciences (ICE), Spanish National Research Council (CSIC), Institut d'Estudis Espacials de Catalunya (IEEC), Barcelona, Spain, where he has been involved in geophysical applications of GNSSs.

**Estel Cardellach** (Senior Member, IEEE) received the Ph.D. degree in physics from the Polytechnic University of Catalonia, Barcelona, Spain, in 2002.

She has been involved in scientific applications of global navigation satellite systems (GNSSs) for remote sensing of the Earth. In 2003, she was an NRC Post-Doctoral Researcher with the NASA/Jet Propulsion Laboratory, Pasadena, CA, USA, and a Post-Doctoral Researcher with the Harvard–Smithsonian Center for Astrophysics, Cambridge, MA, USA, in 2004. Since 2005, she has been with the Institute of Space Sciences (ICE), Spanish National Research Council (CSIC), Institut d'Estudis Espacials de Catalunya (IEEC), Barcelona.

Dr. Cardellach is a Principal Investigator of the spaceborne experiment Radio Occultations and Heavy Precipitation (ROHP) aboard the PAZ Low Earth Orbiter and the Vice-Chair of the Science Advisory Group for the scout mission of the European Space Agency (ESA), HydroGNSS.

**Serni Ribó** (Member, IEEE) received the M.S. degree in telecommunications engineering and the Ph.D. degree from the Polytechnic University of Catalonia, Barcelona, Spain, in 1999 and 2005, respectively.

In 2000, he joined the European Space Agency (ESA), Noordwijk, The Netherlands, with a grant from the Spanish Ministry of Science and Technology, where he was involved in synthetic aperture radiometry technology. Since 2003, he has been with the Institute of Space Sciences (ICE), Spanish National Research Council (CSIC), Institut d'Estudis Espacials de Catalunya (IEEC), Barcelona. He is currently involved in the development of new ocean altimetry and scatterometry global navigation satellite system (GNSS) reflection instrumentation.

**Antonio Rius** received the Ph.D. degree from the University of Barcelona, Barcelona, Spain, in 1974.

From 1975 to 1985, he was a member of the Technical Staff at NASA's Deep Space Communications Complex, Madrid, Spain, where he was responsible for the radio astronomical activities. Since 1986, he has been with the Spanish National Research Council (CSIC), Barcelona. He is currently a CSIC Research Professor AH with the Research Group on Earth Observation, Institut d'Estudis Espacials de Catalunya (IEEC), Barcelona.